

UC Berkeley

UC Berkeley Previously Published Works

Title

Efficiency optimization of microchannel plate (MCP) neutron imaging detectors. 1. Square channels with B-10 doping

Permalink

<https://escholarship.org/uc/item/49m25511>

Journal

Nuclear Instruments & Methods in Physics Research Section A-Accelerators Spectrometers Detectors and Associated Equipment, 539(1-2)

ISSN

0168-9002

Authors

Tremsin, A S
Feller, W B
Downing, R G

Publication Date

2005-02-01

Peer reviewed

Efficiency optimization of microchannel plate (MCP)

neutron imaging detectors:

I. Square channels with ^{10}B doping.

Anton S. Tremsin^{a,*}, W. Bruce Feller^b, R. Gregory Downing^b

^aSpace Sciences Laboratory, University of California at Berkeley

Berkeley, CA 94720, USA

^bNOVA Scientific, Inc. 660 Main St. P.O. Box 928 Sturbridge, MA 01566, USA

Abstract

Microchannel plate (MCP) event-counting imaging detectors with very high spatial resolution ($\sim 10\ \mu\text{m}$) and timing accuracy ($\sim 100\ \text{ps}$) are widely employed for the detection and imaging applications of electrons and ions, as well as UV and X-ray photons. Recently it was demonstrated that the many advantages of MCPs are also applicable to neutron detection with high 2-dimensional spatial resolution. Boron, enriched in the isotope ^{10}B , was added to the MCP glass structure to enhance the neutron interaction within the MCP through the $^{10}\text{B}(n,\alpha)^7\text{Li}$ reaction. The energetic charged particle reaction products release secondary electrons directly into MCP channels, initiating an electron avalanche and a subsequent strong output pulse. In this paper we present a detailed model for calculating the quantum detection efficiency of MCP neutron detectors incorporating

* Corresponding author.

E-mail address: ast@ssl.berkeley.edu (A.S.Tremsin)

^{10}B , for the specific case of square channel MCP geometry. This model predicts that for thermal neutrons (0.025 eV), MCP detection efficiencies of up to 78% are possible using square channels. We also show theoretically that square channel MCPs should have a very sharp (~ 17 mrad) angular drop in sensitivity for detection of normal incidence neutrons, opening up new possibilities for angle-sensitive neutron imaging as well as collimation. The calculations can be used to optimize MCP neutron detection efficiency for a variety of applications. In a subsequent companion paper, the model will be extended to the case of hexagonally-packed circular channels.

Keywords: Neutron detection, Detection efficiency, Neutron imaging

1. Introduction

In the present paper we study the detection efficiency for thermal neutrons based on neutron-to-charged particle conversion in ^{10}B -doped microchannel plates (MCPs) with square channels. Fraser and Pearson [1],[2] first suggested that the direct addition of boron into the MCP glass structure could substantially enhance MCP neutron sensitivity, while simultaneously preserving the many beneficial features of MCP imaging detectors. Later we implemented this concept and then experimentally confirmed it, using cold and thermal neutron beams at the NIST research reactor [3]. Recently, this work was extended to encompass related but more novel detector structures, such as the microsphere plate (MSP), Nova ‘microfiber’ plate (MFP), and the second generation Nova ‘microreticulated’ plate (MRPTM).

In the MCP neutron detection method, the neutron-induced nuclear reaction - $^{10}\text{B}(n,\alpha)^7\text{Li}$ - occurs within few micron-thin glass channel walls, which contain at least several percent by weight of ^{10}B . The alpha and ^7Li charged particle reaction products, moving 180° apart to conserve momentum, emerge from the channel wall surfaces into an open channel. As these heavy particles cross the surface, a relatively large number of secondary electrons and other species [4] (H^{-+} , OH^{-} , ...) are liberated to generate a strong electron avalanche and output pulse in the usual manner [5]. Moreover, once within an open channel, an energetic alpha or ^7Li particle will interact *twice* with a channel wall surface – first upon entry into the channel, and then again after crossing the evacuated channel to strike the opposite wall – virtually insuring the generation of a detectable output pulse [1]. Thus, the useful detection characteristics of MCPs can be very effectively applied to neutron detection and imaging, with position sensitivity on the order of $10\ \mu\text{m}$ and timing accuracy down to $\sim 100\ \text{ps}$ [6],[7].

In the present paper, we focus on the efficiency of neutron detection using ^{10}B -doped MCPs, for both the case of single neutrons where precise interaction coordinates within the channel wall can be assigned, as well as the case of a neutron beam where an averaging process may be used.

Finally, in the interest of brevity this paper is limited to the square pore MCP geometry. This is due to the relatively straightforward solid geometry of square packing, as compared with the greater complexities of hexagonally-packed cylinders or circular channels for the interaction with the spherical geometry of escape of alpha and ^7Li

reaction products. Given the lack of commercially available square channel MCPs at present, and the universal availability of circular channel MCPs, a companion paper for the latter geometry is also being prepared.

2. Neutron detection efficiency for a single neutron

The neutron detection efficiency Q_n of a ^{10}B -doped MCP detector is given by the product of three terms,

$$Q_n = P_1 * P_2 * P_3 \quad (1)$$

where P_1 is the fraction of incident neutrons absorbed by the MCP structure, P_2 is the fraction of those interactions that generate an electron avalanche within an MCP channel, and P_3 is the fraction of avalanches actually registered by the readout electronics system. However, the primary detection process consists of the multiplication of the first two terms P_1 and P_2 . For the first term P_1 , we calculate the probability of neutron absorption and interaction through the reaction $^{10}\text{B}(n,\alpha)^7\text{Li}$ within the bulk MCP glass composition (Section 2.1). Competing radiation reactions in the matrix are considered negligible in this work, although strictly this depends upon the exact glass composition and radiation present. The second term P_2 addresses the escape into an open channel of at least one of the reaction products (Section 2.2). We assume that, once created, an electron avalanche always yields a detectable electron pulse. This implies that $P_3 = 1$. Obviously, this latter assumption is contingent upon details of MCP detector operation, such as use of appropriate bias voltages, the use of multiple MCPs in ‘converter/amplifier’ configuration, as well as the provision of adequate gain and dynamic range for the pulse readout electronics. In practice, judicious care in optimizing these factors can indeed be

In most solid neutron detection schemes, P_1 increases as the density of absorber nuclei increases – but usually at the expense of a corresponding decrease in P_2 , due to the rather limited range (several microns) of the reaction products. In sharp contrast MCP neutron detection is highly unique, in that its microscopic structure can circumvent this problem, through use of micron-thin walls alternating with open channels (Fig. 1).

Given the MeV energies of the alpha and ${}^7\text{Li}$ particles, we can assume that at least several electrons (and possibly other species, such as $\text{H}^{+/-}$, OH^- , etc.) are emitted from one or both MCP channel walls that are struck, and that these secondaries will subsequently be multiplied along the channel. Indeed, it has been shown that for singly charged He^+ ions with energies over a few keV there is at least one induced electron emitted from the MCP glass wall [8],[9]. These authors also report that ions with a higher energy induce the emission of multiple electrons from the MCP glass. Assuming the MCP axial accelerating field is sufficiently strong (~ 1 kV/mm), so that each secondary electron striking the MCP wall has an energy above the threshold value of about 20-30 eV [10], an avalanche of electrons will subsequently be produced. Standard photon or particle-counting MCP detectors operate at gains of about 10^6 - 10^7 , and various readout options have been developed depending upon the specific combination of detector parameters desired (such as counting rate, spatial resolution requirements, need for multi-particle detection, etc.). All these widely used methods can be applied to neutron detection - given that subsequent to the initial neutron detection event, the MCP detection process is essentially the same.

Aside from the dominating issues of neutron absorption, interaction, and secondary particle escape and avalanche formation within MCPs, there may of course be secondary issues concerned with, for example, the generation and detection within the MCP structure of prompt gamma rays from neutron interactions, as well as the ultimate disposition of the Q-value energy in terms of thermal dissipation. For purposes of this paper, these are considered of much lesser significance and are neglected in the following discussion.

Before describing the square channel model, we first consider why this is the optimal MCP geometry for maximizing neutron detection efficiency. Fig. 2 shows two-dimensional (2D) projections of various MCP channel formats: circular, hexagonal and square. Upon inspection, MCPs with circular channels would appear to have a lower escape probability for the reaction products into open channels. A 2D projection shows that there is a larger area corresponding to the “no-escape” zone, as compared with a square or hexagonal channel geometry. In the 3D case, the relative volume of the no-escape zone for a circular channel geometry is higher. For hexagonal channels, the escape probability lies somewhere between the probabilities for circular and square channels. However, the efficiency of neutron absorption would still be higher for the circular channel case. Indeed, the total detection efficiency (proportional to the product of probabilities of neutron absorption and alpha or ${}^7\text{Li}$ escape into an MCP pore) can be shown to be lower for circular channels, as most of the increase in the absorption probability is due to areas where the escape probability is zero. Furthermore, a square channel MCP can still have the same absorption efficiency as a circular channel MCP,

provided the thickness L_{MCP} of the square-pore MCP is increased. On the other hand, a lower escape probability in a circular channel geometry cannot similarly be compensated. We thus focus our attention on square channels in our initial model for calculating MCP neutron detection efficiency – not only because it is simpler to treat mathematically – but also because it has the most efficient MCP channel geometry, as compared with circular and hexagonal channels. We are currently evaluating a square channel microchannel plate, where every other row is shifted by half a channel width. This MCP geometry design is even more efficient in terms of detection efficiency for reasons that will become obvious later in this paper.

2.1. Probability P_1 of neutron absorption

The probability that a neutron is absorbed inside an MCP is given by [2]

$$P_1 = 1 - \exp(-N_{^{10}\text{B}}\sigma L_{eff}) \quad (2)$$

where $N_{^{10}\text{B}}$ is the number of ^{10}B atoms per unit volume of the MCP structure, σ is the cross section for the ^{10}B (n, α) reaction, and L_{eff} is the effective path length of a neutron inside the MCP. It is well known that σ is a function of neutron energy, is generally inversely proportional to the neutron velocity [11]), and for ^{10}B , is essentially structureless - at least up to fast neutron energies (~500 keV). For thermal neutrons having an energy 0.025 eV, the cross section is 3837 barns, with the isotope ^{10}B constituting 19.9% of natural boron. Method of calculation of parameters $N_{^{10}\text{B}}$ and L_{eff} is described in Appendixes A and B.

2.1.1. *Stacking MCPs to attain greater neutron absorption*

To attain the highest possible MCP detection efficiency for neutrons, the initial goal in the detection process should be the attainment of near-unity interaction probability in the MCP glass structure. Here, the MCP must be made sufficiently thick in combination with a high number density of ^{10}B atoms in the glass to absorb essentially all incident neutrons. Obviously, single MCP thickness cannot be increased indefinitely, given the simultaneous requirements that channel walls be made as thin as possible (to permit reaction product escape into open channels, discussed below in Sect. 2.2), and that appropriate channel length-to-diameter (L_{MCP}/d) ratios are limited within the range of $L_{MCP}/d \sim 40$ to 175. The L_{MCP}/d constraint is due to considerations of the physics of the channel electron multiplication process, as well as pragmatic manufacturing issues. Extensive studies carried out in the past show that L_{MCP}/d ratios ranging from 40-60 (for optimized ‘analog’ imaging) to 80-175 (for pulse counting free of ion feedback noise) essentially bracket the working limits of effective MCP operation. MCP manufacturing processes add their own constraints; for example, the chemistry of the acid core-etch process or corrosion reaction, which rapidly becomes unfavorable due to the increasing channel internal surface to volume ratio as channel diameters approach only a few microns. Finally, there are pragmatic device mounting issues, where the handling of voltage levels of several thousand volts across very thin sub-mm glass wafers becomes a formidable task.

For all these reasons, it becomes attractive to simply stack several MCPs together, in the widely used chevron or Z-stack arrangement [5]. Not only are pulse-counting gain

levels of $\sim 10^6$ to 10^7 reached, allowing electronic imaging readout methods to be used, but total neutron absorption is also increased, as determined by the overall MCP thickness. At the same time, the two or more detectors can be stacked (see Fig. 3) in order to increase the absorption efficiency to virtually 100%, as used commonly with other neutron detection devices. The grids collecting signal electrons, shown in Fig. 3, can be replaced by a position-sensitive anode made of materials nominally transparent to neutrons, thus providing position sensitivity in the stacked detector.

Finally, gamma rays and minimum ionizing particles (e.g., cosmic ray muons) produce weak interactions via the photoelectric effect, Compton effect or pair production, and scales with MCP thickness with a detection efficiency of $\sim 1-2\%$ per mm [12] for most channel geometries. At first glance, this might seem attractive as the $^{10}\text{B}(n,\alpha)^7\text{Li}$ reaction yields a 0.48 MeV gamma ray (94% branching ratio) when the excited lithium nucleus quickly (~ 0.1 ps) returns to its ground state. This event would only add to the detection efficiency. However, this addition would be quite insignificant compared with the signal from the alpha particle and ^7Li reaction products. Thus simply increasing MCP thickness may not be a desirable approach, particularly in sensitive neutron detection applications where minimizing the simultaneous detection sensitivity of gammas is critical. In some neutron detection applications, a relatively high flux gamma ray field may accompany the neutron signal, creating a background interference. The competing requirements of maximum bulk neutron absorption with minimum bulk gamma absorption can therefore work at cross purposes. Neutron-gamma discrimination using techniques such as pulse analysis or fast timing, commonly employed with other solid-

state neutron detection schemes [13], and the separation of neutron capture and electron multiplication in front- and back-MCPs [14] are currently under investigation.

2.2. Escape probability P_2 of ^4He and ^7Li nuclei reaction products

A reaction product, either an alpha or ^7Li particle, has to escape into an open MCP channel to initiate an electron avalanche. If both the alpha and the ^7Li escape into a channel, only one of them needs be taken into account, since either particle corresponds to the same neutron capture event. Therefore, we first calculate the higher probability of alpha escape into an MCP channel and then consider those ^7Li particles cases where the associated alpha is completely absorbed by the MCP glass (i.e., does not escape into an open channel).

In the present model, we assume that if neutron absorption inside an MCP wall happens within the escape range from the pore, then the alpha (and/or ^7Li) particle escapes into the MCP pore and produces an electron avalanche with unit probability. This assumption corresponds to the lowest estimate of probability P_2 . Secondary effects leading to electron cascades, due to knock-on particles, induced x-ray emission, reaction gamma, etc. are ignored. The ranges of alpha and ^7Li particles depend on their energies; for the current neutron-sensitive MCP glass compositions developed by Nova, the escape ranges R_1 are approximately 3.54 μm for 1472 keV and 4.23 μm for 1777 keV alpha, while for ^7Li the ranges R_2 are 1.91 μm and 2.15 μm for 838 and 1014 keV ^7Li . Values were calculated using SRIM 2000, The Stopping and Range of Ions in Matter, a set of computer programs developed through the works of Ziegler, et al. [15]. For simplicity the

modeled detection efficiency presented in this paper uses "averaged" escape ranges of $R_1=3.54$ and $R_2=2 \mu\text{m}$.

Assigning position coordinates (X,Y) to the point of neutron interaction, we first calculate P_2^α - the probability of escape into a channel for the alpha particle, then add the escape probability P_2^{Li} of a ${}^7\text{Li}$ particle corresponding to an alpha that is absorbed by the channel wall:

$$P_2(X,Y) = P_2^\alpha(X,Y) + P_2^{\text{Li}}(X,Y) \quad (3)$$

The emission of the alpha and ${}^7\text{Li}$ reaction products is isotropically distributed from the point of a thermal neutron interaction. Another key feature of the MCP neutron capture process is the fact that alpha and ${}^7\text{Li}$ particles are emitted diametrically. Therefore we can precisely calculate the probability P_2^{Li} , corresponding to those ${}^7\text{Li}$ particles associated with alpha particles absorbed by the channel wall glass. A detailed description of our model for calculating parameters $P_2^\alpha(X,Y)$ and $P_2^{\text{Li}}(X,Y)$ is described in Appendix C.

3. Averaged probability of neutron detection

The probability of single neutron detection, as described in Sect. 2, depends upon the position (x_0,y_0) of neutron impact upon the MCP surface, and angle (θ,φ) of the trajectory relative to the MCP axis. However, there is also interest in the less demanding case of imaging the flux of relatively intense (10^5 - $10^9 \text{ cm}^{-2} \text{ s}^{-1}$) *beams* of neutrons, such as

in radiography or scattering applications with research reactor sources. In this case, the relevant quantity of interest for assessing detection efficiency will be the averaged probability of neutron detection, which will now be derived.

In section 2.1 we estimated the probability P_1 of neutron absorption with the MCP wall, but not the precise location within the wall where the absorption event occurred. To properly calculate the escape probability P_2 of the alpha and ${}^7\text{Li}$ particle reaction products, we must first know the coordinates (X,Y) of the point of neutron absorption. Obviously, when the neutron is absorbed closer to the wall surface, there is a greater chance for the reaction products to escape into an open channel and to initiate an electron avalanche.

Given a distribution function $\rho_2(X,Y)$ of the neutron absorption within an MCP wall we can calculate the *averaged* probability $\langle P_2 \rangle = \langle P_2(X,Y) \rangle$ that either of the two reaction particles will escape into an open channel:

$$\langle P_2 \rangle = \langle P_2(X,Y) \rangle = \frac{\int dY \int P_2(X,Y) \rho_2(X,Y) dX}{\int dY \int \rho_2(X,Y) dX} \quad (4)$$

For a neutron beam with a uniform intensity distribution on the scale of 10-15 μm (MCP pitch) (that is, to ignore effects of self shielding) the distribution function $\rho_2(X,Y)$ can be assumed to be a constant (the coordinates (X,Y) of the neutron absorption can be assumed *uniformly distributed within the MCP walls*, typically a few μm thick). Subsequently the integral of (4) becomes:

$$\langle P_2(X, Y) \rangle = \frac{\frac{d}{2} \frac{W}{2} \langle P_2^I(X, Y) \rangle + \frac{1}{2} \frac{W^2}{4} \langle P_2^{II}(X, Y) \rangle}{dW/4 + W^2/8} = \frac{2 \int_0^{d/2} dY \int_0^{W/2} P_2(X, Y) dX + \int_{d/2}^{(d+W)/2} dY \int_0^{W/2} P_2(X, Y) dX}{(2d+W)W} \quad (5)$$

The averaging of (5) is carried out over areas I and II, which are shaded in Fig. 4. By symmetry, any position X, Y within the channel wall can be represented by a corresponding point within the shaded area, where there are two regions: Region I, inside the wall parallel to the Y-axis (where $0 \leq Y < d/2$) and denoted by $(P_2^I(X, Y))$, and Region II, inside the intersection between this wall and the perpendicular wall ($d/2 \leq Y < (d+W)/2$), aligned with the X-axis, and denoted by $(P_2^{II}(X, Y))$. The averaged probabilities $\langle P_2^I(X, Y) \rangle$ and $\langle P_2^{II}(X, Y) \rangle$ in (5) are normalized by the corresponding area, to obtain the total averaged escape probability $\langle P_2(X, Y) \rangle$. Finally, the total averaged detection efficiency is given by

$$\langle P \rangle = \langle P_1(x_0, y_0) \rangle \langle P_2(X, Y) \rangle P_3 \quad (6)$$

For a highly-collimated (parallel) neutron beam normally incident ($\theta = \pi/2$) to an MCP with zero degree channel bias (i.e., channels normal to the MCP input face) the averaged probability $\langle P_1(x_0, y_0) \rangle$ is found from:

$$\langle P_1(x_0, y_0) \rangle = \frac{(W+2d)W}{(W+d)^2} P_1|_{L_{\text{eff}}=L_{\text{eff}}\left(\frac{W}{2}, \frac{W}{2}, \frac{\pi}{2}, 0\right)}. \quad (7)$$

For the case of non-normal neutron incidence (θ between θ_{\min} and θ_{\max}), and given that essentially all neutron beams used in research have a width greater than 10-15 μm (the MCP pore-to-pore period), we can continue to assume that the coordinates (X, Y) for neutron absorption are uniformly distributed (due to the finite thickness of the MCP walls

and large aspect ratio L_{MCP}/d). Thus (5) and (6) can still be used to obtain the averaged detection efficiency, whereas (7) cannot be used. Instead, a more comprehensive averaging can be substituted for the latter, using integration to obtain $\langle P_1 \rangle$:

$$\langle P_1 \rangle = \langle P_1(x_0, y_0, \theta, \pi) \rangle = \frac{\int_0^{d+W} dx_0 \int_0^{d+W} dy_0 \int_{\theta_{\min}}^{\theta_{\max}} d\theta \int_{\varphi_{\min}}^{\varphi_{\max}} P_1(x_0, y_0, \theta, \varphi) \rho I(x_0, y_0, \theta, \varphi) d\varphi}{\int_0^{d+W} dx_0 \int_0^{d+W} dy_0 \int_{\theta_{\min}}^{\theta_{\max}} d\theta \int_{\varphi_{\min}}^{\varphi_{\max}} \rho I(x_0, y_0, \theta, \varphi) d\varphi} \approx \frac{\int_{\theta_{\min}}^{\theta_{\max}} d\theta \int_{\varphi_{\min}}^{\varphi_{\max}} \rho I(\theta, \varphi) d\varphi \int_0^{d+W} dx_0 \int_0^{d+W} P_1(x_0, y_0, \theta, \varphi) dy_0}{\int_{\theta_{\min}}^{\theta_{\max}} d\theta \int_{\varphi_{\min}}^{\varphi_{\max}} \rho I(\theta, \varphi) d\varphi} \quad (8)$$

where $\rho I(x_0, y_0, \theta, \varphi)$ is the distribution function for incident neutrons. The simplification evident in (8) is again based on the assumption that the neutron beam is larger than the channel pitch, and that the function $\rho I(x_0, y_0, \theta, \varphi)$ is assumed constant within the limits of integration for coordinates $(x_0, y_0) \in [0, d+W]$, so that $\rho I(x_0, y_0, \theta, \varphi) \approx \rho I(\theta, \varphi)$.

4. Model predictions

The neutron detection efficiency is a parameter of great interest in most neutron detection applications, particularly at low neutron fluence. Until recently, MCPs have been optimized for the sensitive detection of many other types of particles – electrons, ions, and especially photons in the spectral range extending from soft X-ray wavelengths down to the visible, where photocathodes are usually employed. The individual MCP channel input surfaces (in some cases coated with a photocathode) convert incident

particles into secondary electrons, which then develop electron cascades and detectable pulses. For neutrons, the MCP bulk material itself acts as an analogue ‘photocathode’ or converter, where an incident neutron is converted by boron absorption into secondary ionizing particles that then enter the MCP channels, liberating further secondary particles (e.g., electrons, protons, OH⁻ ions, etc.) that then create electron cascades and output pulses.

As described earlier, the efficiency of this conversion process depends upon the product $P_1 * P_2$ - the probability P_1 of neutron absorption in the MCP glass walls that are doped with ¹⁰B atoms and the subsequent probability of escape into a channel, P_2 , of at least one of the alpha or ⁷Li charged particles. We use this model to derive expressions for P_1 and P_2 to allow prediction of absolute MCP neutron detection efficiencies, optimized through careful choice of MCP parameters such as channel dimensions d , and channel pitch or spacing (hence wall thickness W), and the overall MCP thickness L_{MCP} . Also important is the level of boron-doping incorporated in the alkali lead silicate glass, which is constrained by complex and exacting fiber draw and MCP fabrication processes.

Obviously, there can be severe constraints on variations allowed in the structural variables of MCPs (e.g., d , W , and L_{MCP}), including allowances for proper electrical operation, issues involving mechanical strength, and even issues of cost. For example, it is desirable to minimize the channel wall thickness in order to maximize the escape probability P_2 of the reaction products. However, the MCPs having the thinnest channel walls, corresponding to the smallest channel diameters (2 microns, available commercially from Burle [16]), represent a considerable technological achievement in its own right, given the fragility of submicron glass channel walls and the very high applied

fields (~ 10 kV/mm) that must be sustained across the MCP glass, needed to accelerate secondary electrons above the first crossover potential (~ 20 eV) before striking the opposing channel wall [10]. Unfortunately, one of the essential MCP manufacturing steps of acid core etch becomes essentially impossible for large L_{MCP}/d ratios ($>500:1$), especially given the presence of boron, which only increases acid solubility. Various tradeoffs and compromises in MCP design must be made. Therefore, the simulation results presented in this section correspond to a reasonable set of MCP parameters realistically attainable with current manufacturing practices, and assume a level of ^{10}B doping of 10 mole percent.

4.1. Probability of neutron absorption P_1

The probability of neutron absorption P_1 for a single neutron is a function of neutron path inside the MCP glass walls L_{eff} , (2). Fig. 5 shows the portion of L_{eff} relative to MCP thickness L_{MCP} as a function of incidence angle θ for fixed angles φ . The point of neutron incidence (x_0, y_0) in these calculations was chosen to be in the center of the MCP wall. The path of neutron travel within the MCP glass quickly reaches (within a few degrees) the value equal to $(1 - A_{open})$, where $A_{open} = W^2/(d+W)^2$ and is the open area of the MCP ($A_{open} = 64\%$ for the case of the MCP modeled in Fig. 5). There are exceptions at angles $\varphi = 0, 90, 180$ and 270 degrees, when the neutron always travels within the MCP glass if the incidence point (x_0, y_0) lies on the MCP wall. The probability of neutron absorption P_1 averaged over incidence points (x_0, y_0) as a function of incidence angle θ (for fixed angles φ) is shown in Fig. 6. The averaging was performed assuming that the spatial distribution of the incident neutron beam was uniform within $10 \mu\text{m}$. The

absorption probability is essentially independent of angle φ , except for the special cases $\varphi = 0, 90, 180$ and 270 degrees. P_1 reaches a plateau within a few degrees relative to the MCP normal. The efficiency of neutron detection consequently exhibits a sharp drop, when the MCP pore axis coincides with the axis of neutron incidence whenever the neutron beam is collimated to within d/L_{MCP} radians.

Our experimental measurements of neutron absorption [17], performed with microchannel plates with circular pores support the validity of the absorption part of our model. The results of the absorption probability calculations for an MCP with $8 \mu\text{m}$ pores on $11.5 \mu\text{m}$ centers based on the model described in Section 2.1 (modified for circular-pore geometry) agree with the experimental data obtained at the neutron guide beam line (NG-0) at the National Institute of Standards and Technology, a neutron beam with average energy of 5 meV . In the near future we hope to produce neutron collimators with good angular selectivity by substantially increasing the MCP aspect ratio (L_{MCP}/d).

Fig. 7 presents the calculated averaged probability of neutron absorption P_1 as a function of both angles θ and φ for square-pore MCP (the same MCP as in Fig. 5 and Fig. 6). In Fig. 7.a there is no correction for the MCP area loss due to MCP tilt relative to the incident neutron beam (the width of the neutron beam is much smaller than the MCP width), while the same data corrected for $\sim \sin(\theta)$ area loss is shown in Fig. 7.b (corresponding to the case when the width of the neutron beam is comparable or larger than the MCP width). In both cases variation in P_1 is quite small for the incidence angles

θ in the range of 70° to 88° . Note the 4-fold symmetry along the φ -axis seen in these figures, which can be attributed to the invariance of MCP geometry to 90° rotations.

The stacking of three boron-doped MCPs obviously does not lead to a threefold increase of absorption probability P_1 , since the second MCP detects only those neutrons not detected by the first MCP. However, a stack of only three 1 mm thick MCPs with 8 μm pores (which can be manufactured using current technology) increases the absorption probability from 0.52 to 0.9 (see Fig. 8). The results shown in Fig. 8 correspond to a stack of three MCPs identical to the ones simulated in Fig. 5 and Fig. 6. Thus 90% of thermal neutrons should be absorbed within the MCP glass for a stack of three 125:1 L_{MCP}/d , 8 μm pore and 2 μm wall MCPs with currently achievable level of 10 mole percent ^{10}B doping.

4.2. Escape probability P_2 of alpha and/or ^7Li particles

The probability P_2 that at least one of the particles produced in the neutron-boron reaction escapes into an MCP pore is clearly a function of MCP wall thickness. The thinner the walls, the larger the probability P_2 . Depending on application, an appropriate combination of MCP structural parameters can be chosen, with the thickness of MCP walls d and the MCP pore width W among them. We start the simulation with the function $P_2^\alpha(X,Y)$ from (44) for an MCP with 8 μm pores and 2 μm walls. Fig. 9 shows the escape probability for alpha particles (solid line) as a function of y_0 position along the MCP wall with a fixed value of x_0 (depth within the wall, see Fig. 4). $P_2^\alpha(X,Y)$ decreases from 0.7 to 0.5 as the neutron capture point moves closer to the pore corner ($y_0 = 4 \mu\text{m}$) and then stays the same in region II of Fig. 4. This is because the radius of the escape

sphere (R_l , the range for alpha particles) is larger than the wall thickness W . Our model accounts for both emission to the left pore and emission to the right pore. There is no significant change of probability $P_2^\alpha(X,Y)$ with variation of position x_0 within the wall (Fig. 9.a, Fig. 9.b, Fig. 9.c), except for the region close to the pore corner ($3 \mu\text{m} < x_0 < 4 \mu\text{m}$) for the same reason that W is smaller than R_l .

The dashed line in Fig. 9 represents the probability $P_2^{\text{Li}}(X,Y)$ of ${}^7\text{Li}$ particle escape into an MCP pore, only for the case when an alpha is absorbed in the MCP wall glass. Those are the only particles that result in separate events, contributing to the total probability of neutron detection P_2 . From Fig. 9, $P_2^{\text{Li}}(X,Y)$ has a strong dependence on both x_0 and y_0 positions of the neutron capture reaction. The closer x_0 is to the MCP wall, the larger the contribution of ${}^7\text{Li}$ particles to the detection process, since more alpha particles (which are emitted into the opposite pore) are absorbed in the MCP glass. Thus the total probability of neutron detection $P_2(X,Y)$ increases as the neutron is absorbed closer to the MCP wall surface. More detailed information on the dependence of escape probability from both x_0 and y_0 for the same MCP geometry is shown in Fig. 10-Fig. 12.a. The dark area in the insert in Fig. 10 shows the region of the MCP wall for which the data are presented. The probability $P_2(X,Y)$ of at least one particle escaping into a pore reaches unity, when a neutron is absorbed far from the corner (away from the perpendicular wall) and close to the wall surface. The minimum of $P_2(X,Y)$ is correspondingly in the middle of the MCP wall crossover. Fig. 12.b shows simulation results for an MCP with a pore diameter and wall thickness that is twice as large as that depicted in Fig. 11.a.

Once the functions $P_2^\alpha(X,Y)$ and $P_2^{Li}(X,Y)$ are known, it is possible to calculate the averaged escape probabilities P_2^α and P_2^{Li} from (5) and thus find the second term (P_2) of (1) required for the calculation of the neutron detection efficiency of a ^{10}B -doped MCP detector. For the reasons explained in Section 3, functions $P_2^\alpha(X,Y)$ and $P_2^{Li}(X,Y)$ should be averaged over regions I and II (Fig. 4), in order to find $\langle P_2 \rangle$. The averaged escape probabilities for alpha and ^7Li particles are presented in Fig. 13 and Fig. 14 as functions of the MCP pore width d and the wall thickness W . When the MCP pore width is a few times larger than the wall thickness, the alpha particle escape probability is not a strong function of pore width; this probability decreases with the increase of the wall thickness W . On the other hand, the contribution from ^7Li recoil particles has its maximum at a wall thickness W corresponding to 4 μm , but this contribution does not exceed about 22% for the range of parameters d and W under consideration.

The averaged escape probability P_2 as a function of both parameters, d and W (Fig. 15.a), and as a function of the pore width d only (with wall thickness fixed, Fig. 15.b), thus indicates that rather high neutron detection efficiencies can clearly be achieved. The escape probability P_2 for an MCP having 8 μm pores with 2 μm walls (as is typical for current commercial MCP devices), can even be as high as $\sim 78\%$. Taking into account the fact that the absorption probability P_1 can approach unity (for a stacked detector configuration, Section 2.1.1) and the fact that the probability of generating an electron avalanche P_3 can be close to unity (see Section 2), it is evident that very efficient neutron counting using MCP-based detectors with high spatial resolution ($\sim 10 \mu\text{m}$) and sub-nanosecond timing capability becomes feasible.

Acknowledgements

The authors would like to thank George Lamaze, Heather Chen-Mayer, and David Mildner of the NIST Nuclear Methods Group for assistance in the early experiments confirming the effectiveness of boron-doped MCPs and his help with the manuscript. We also thank Paul White of Nova Scientific, George Fraser of the University of Leicester, Richard Lanza of MIT, and Oswald Siegmund of the Space Sciences Laboratory, University of California at Berkeley for their involvement at various levels.

Appendix A

Number density of ^{10}B atoms in MCP glass

The number of boron atoms per cm^3 in MCP glass can be found using

$$N_{^{10}\text{B}} = 2 \frac{\rho_{\text{glass}} * \%m_{\text{B}_2\text{O}_3}}{M_{\text{B}_2\text{O}_3}} \quad (9)$$

where ρ_{glass} is the MCP glass density, $\%m_{\text{B}_2\text{O}_3}$ and $M_{\text{B}_2\text{O}_3}$ are respectively the mass percentage of B_2O_3 molecules in the glass and the mass of one B_2O_3 molecule. $\%m_{\text{B}_2\text{O}_3}$

can be found from the formula $\%m_{\text{B}_2\text{O}_3} = \frac{m_{\text{B}_2\text{O}_3} \mu_{\text{B}_2\text{O}_3}}{\sum_i m_i \mu_i}$, where the denominator is the

effective atomic weight, summed over all glass constituents and approximately equal to 90 for typical commercial MCP glasses. $m_{\text{B}_2\text{O}_3}$ and $\mu_{\text{B}_2\text{O}_3}$ are, respectively, the atomic mass of a B_2O_3 molecule and the mole fraction of B_2O_3 in the glass. The number of boron atoms per unit volume in MCP glass can therefore be found from

$$N_{10B} = 2 \frac{\rho_{glass} m_{B_2O_3} \mu_{B_2O_3}}{M_{B_2O_3} \sum_i m_i \mu_i} \quad (10)$$

Appendix B

L_{eff} - effective length of neutron path within the MCP structure

We will calculate the neutron absorption path length through the MCP as a function of position and angle, $L_{eff} = L_{eff}(x_0, y_0, \theta, \varphi)$. This is essentially determined by the integrated path length within MCP channel walls, since traversal of open channels, does not contribute to absorption. We start with the assumption that a neutron lands on the MCP input surface at point (x_0, y_0) with angles of incidence θ and φ as shown in Fig. 16. Depending upon parameters $(x_0, y_0, \theta, \varphi)$, a neutron crosses multiple MCP channels as it travels from the MCP input to output surface. For normal incidence, where $\theta = \pi/2$, the effective path length $L_{eff} = L_{MCP}$ if (x_0, y_0) lies within an MCP wall; otherwise, $L_{eff} = 0$ if (x_0, y_0) is within the MCP open channel. We have

$$L_{eff}(x_0, y_0, \theta, \varphi) = \begin{cases} 0; & \theta = \pi/2, \quad W \leq x'_0 \leq W + d \quad \text{and} \quad W \leq y'_0 \leq W + d \\ L_{MCP}; & \theta = \pi/2, \quad 0 < x'_0 < W \quad \text{or} \quad 0 < y'_0 < W \\ L1_{eff}; & \theta \neq \pi/2 \end{cases} \quad (11)$$

where d and W respectively refer to the MCP channel width and wall thickness. The value $L1_{eff}$ for the case where $\theta \neq \pi/2$ is given by

$$L1_{eff} = \frac{L_{MCP}}{\sin \vartheta} \left(1 - \sqrt{\frac{(S_x^{(pore)})^2 + (S_y^{(pore)})^2}{(x'_1 - x'_0)^2 + (y'_1 - y'_0)^2}} \right) \quad (12)$$

where $S_x^{(pore)}$ and $S_y^{(pore)}$ are respectively the projections along the x, y coordinate axes of the neutron path inside the MCP pore or channel (Fig. 17), whereas $(x'_1 - x'_0)$ and $(y'_1 - y'_0)$

are the projections of the *total* neutron path (i.e., channel plus wall). Points (x_0', y_0') and (x_1', y_1') are, respectively, the starting point and endpoint of neutron travel within the MCP, with the origin chosen such that the range of both x_0' and y_0' is always $[0, W+d]$.

Thus

$$x_0' = x_0 - \text{int}\left(\frac{x_0}{W+d}\right) * (W+d) \quad (13.a)$$

$$y_0' = y_0 - \text{int}\left(\frac{y_0}{W+d}\right) * (W+d) \quad (13.b)$$

$$x_1' = x_0' + L_{MCP} \text{ctg} \theta \cos \varphi \quad (14.a)$$

$$y_1' = y_0' + L_{MCP} \text{ctg} \theta \sin \varphi \quad (14.b)$$

The function $\text{int}(\xi)$ used in eq. (13) is defined as the integer value of a positive real number ξ (without rounding to the closest integer). For negative ξ , it is the negative integer value with 1 subtracted (e.g. $\text{int}(0.877) = 0$, $\text{int}(21.32) = 21$, $\text{int}(-2.14) = -3$, etc.).

Clearly $S_y^{(pore)} = 0$ for $\varphi = 0$ or $\varphi = \pi$, and $S_x^{(pore)} = 0$ for $\varphi = \pi/2$ or $\varphi = 3\pi/2$ (as the neutron travels along x and y-axes, respectively). To find $S_x^{(pore)}$ and $S_y^{(pore)}$ for cases when they are not equal to zero, we will initially determine the minimum and maximum indices of the channels which a neutron crosses during its travel within an MCP,

$$i_{\max} = \text{int}\left(\frac{x_e}{W+d}\right), \quad i_{\min} = \text{int}\left(\frac{x_s}{W+d}\right) \quad (15)$$

$$j_{\max} = \text{int}\left(\frac{y_e}{W+d}\right), \quad j_{\min} = \text{int}\left(\frac{y_s}{W+d}\right) \quad (16)$$

where

$$x_s = \min(x_0', x_1'), \quad x_e = \max(x_0', x_1') \quad (17.a)$$

$$y_s = \min(y_0', y_1'), \quad y_e = \max(y_0', y_1') \quad (17.b)$$

Let us now sum all the projections of the neutron travel within individual channels,

$$S_x^{(pore)} = \begin{cases} 0; & \varphi = \pi/2, 3\pi/2 \\ \sum_{i_{\min}}^{i_{\max}} x_i^{(pore)}; & \varphi = 0, \pi \\ \sum_{i_{\min}}^{i_{\max}} \sum_{j_{\min}}^{j_{\max}} x_{ij}^{(pore)}; & \varphi \neq 0, \pi/2, \pi, 3\pi/2 \end{cases} \quad (18.a)$$

$$S_y^{(pore)} = \begin{cases} 0; & \varphi = 0, \pi \\ \sum_{j_{\min}}^{j_{\max}} y_j^{(pore)}; & \varphi = \pi/2, 3\pi/2 \\ \sum_{i_{\min}}^{i_{\max}} \sum_{j_{\min}}^{j_{\max}} y_{ij}^{(pore)}; & \varphi \neq 0, \pi/2, \pi, 3\pi/2 \end{cases} \quad (18.b)$$

where $x_i^{(pore)}$ and $y_j^{(pore)}$ are projections of the neutron path within individual MCP channels for the simple cases when, respectively, either $S_y^{(pore)}$ or $S_x^{(pore)}$ are equal to zero.

These projections can be found from

$$x_i^{(pore)} = \begin{cases} 0; & x_e < x_i^s \quad \text{or} \quad x_s > x_i^e \quad \text{or} \quad y_s \leq W \\ \min(x_e, x_i^e) - \max(x_s, x_i^s); & x_e > x_i^s \quad \text{and} \quad x_s < x_i^e \quad \text{and} \quad y_s > W \end{cases} \quad (19.a)$$

$$y_j^{(pore)} = \begin{cases} 0; & y_e < y_j^s \quad \text{or} \quad y_s > y_j^e \quad \text{or} \quad x_s \leq W \\ \min(y_e, y_j^e) - \max(y_s, y_j^s); & y_e > y_j^s \quad \text{and} \quad y_s < y_j^e \quad \text{and} \quad x_s > W \end{cases} \quad (19.b)$$

where x_i^s and x_i^e are the left and right boundaries of the i-th MCP channel,

$$x_i^s = (d + W)i, \quad x_i^e = (d + W)i + d \quad (20.a)$$

and y_j^s and y_j^e are the bottom and top boundaries of the j-th MCP channel,

$$y_j^s = (d + W)j, \quad y_j^e = (d + W)j + d \quad (20.b)$$

For the remaining case, when $\varphi \neq 0, \pi/2, \pi, \text{ and } 2\pi/3$, the projections of the neutron path within the ij-th MCP pore $x_{ij}^{(pore)}$ and $y_{ij}^{(pore)}$ are given by

$$x_{ij}^{(pore)} = \begin{cases} \begin{cases} \min[x_e, \min(x_i^e, (y_j^e - b)/k)] - \\ \max[x_s, \max(x_i^s, (y_j^s - b)/k)] \end{cases} & k > 0 \quad \text{and} \quad x_i^e > (y_j^e - b)/k \quad \text{and} \quad x_i^s < (y_j^e - b)/k \\ \begin{cases} \min[x_e, \min(x_i^e, (y_j^s - b)/k)] - \\ \max[x_s, \max(x_i^s, (y_j^e - b)/k)] \end{cases} & k < 0 \quad \text{and} \quad x_i^e > (y_j^e - b)/k \quad \text{and} \quad x_i^s < (y_j^s - b)/k \\ 0; & \text{otherwise} \end{cases}$$

$$y_{ij}^{(pore)} = \begin{cases} \begin{cases} \min[y_e, \min(y_j^e, (x_i^e * k + b))] - \\ \max[y_s, \max(y_j^s, (x_i^s * k + b))] \end{cases} & k > 0 \quad \text{and} \quad x_i^e > (y_j^s - b)/k \quad \text{and} \quad x_i^s < (y_j^e - b)/k \\ \begin{cases} \min[y_e, \min(y_j^e, (x_i^s * k + b))] - \\ \max[y_s, \max(y_j^s, (x_i^e * k + b))] \end{cases} & k < 0 \quad \text{and} \quad x_i^e > (y_j^e - b)/k \quad \text{and} \quad x_i^s < (y_j^s - b)/k \\ 0; & \text{otherwise} \end{cases}$$

where the line represented by $y=kx+b$ corresponds to the neutron travel path in the XY-plane, with coefficients k and b found from:

$$k = \frac{y_1' - y_0'}{x_1' - x_0'}, \quad b = y_0' - kx_0' \quad (21)$$

Having thus found N_{10B} and L_{eff} , we can now calculate the probability of position- and angle-dependent single neutron absorption $P_1 \equiv P_1(x_0, y_0, \theta, \varphi)$ from (2). For sake of brevity, the results of calculations for the probability of a single neutron absorption are intentionally not shown. The probability averaged over all possible incidence positions (x_0, y_0) is discussed in Sections 3 and 4. For most applications it is this averaged probability which characterizes the detector performance since in many applications utilizing neutron beams the beam dimensions are typically much larger than the channel-to-channel spacing (or pitch of MCPs), typically on the order of 10-15 μm .

Appendix C

Escape probability $P_2^\alpha(X, Y)$ and $P_2^{Li}(X, Y)$ of the alpha and ${}^7\text{Li}$ particles

We introduce an imaginary sphere with radius set equal to the particle escape range, with the center at the point of neutron reaction. A portion of the sphere surface (areas 1,3 and 7 in Fig. 18 falls within the MCP channel wall, and corresponds to particles that fail to escape into an open channel, while other portions of the surface fall within the open channel. This corresponds to alpha or ${}^7\text{Li}$ particles that enter into the open channel and initiate an electron avalanche. The probability of alpha or ${}^7\text{Li}$ particle escape into an open MCP channel is the ratio of the sphere surface contained inside an open channel to the total surface area $4\pi R^2$. In the most general case, the escape sphere consists of up to nine separate components (see Fig. 18), discussed in detail in Sections C.1 and C.2. Fig. 18 depicts only one hemisphere of alpha emission, located to the right, while the emission of recoil ${}^7\text{Li}$ is represented by the hemisphere on the left, which has a smaller radius (i.e., ${}^7\text{Li}$ particles corresponding to alphas emitted to the right can only be emitted to the left).

C.1 Escape probability $P_2^\alpha(X, Y)$ of the alpha particle

First we consider the escape probability $P_2^{\alpha(0)}$ for an alpha particle when it is far from the corner of a channel, that is for Y in the range

$$0 \leq Y < d/2 - R_1 \quad (22),$$

where d is the channel width. We limit ourselves here only to positive values of Y , since the equations for negative Y are completely symmetric with respect to the coordinate system origin at the center of the MCP channel wall. The distance to the nearest MCP channel is

$$L^\pm = \frac{W}{2} \mp x \quad (23)$$

where L^+ corresponds to emission to the right, with L^- emission to the left.

For Y as determined by (22), the escape probability is the ratio of that part of the escape sphere $S_{\alpha,0}$, lying within an MCP channel (the combined areas 2, 3 and 4 of Fig. 18 and including portions of the left hemisphere not depicted in the figure) to the total spherical surface $4\pi R^2$. The portion of the sphere lying within an open MCP channel is cut by the plane of a channel wall (either $X=W/2$ or $X=-W/2$). The escape probability then becomes:

$$P_2^{\alpha(0)}(X, Y) \equiv P_2^{\alpha(0)}(X) = \frac{1}{4\pi R_1^2} [S_{\alpha,0}^+(X) + S_{\alpha,0}^-(X)] \quad (24)$$

where

$$S_{\alpha,0}^\pm(X) = F(L^\pm(X), R_1) \quad (25)$$

$$F(L, R) = \begin{cases} 2\pi R^2 \left(1 - \frac{L}{R}\right); & L < R \\ 0, & L \geq R \end{cases} \quad (26)$$

There is no particle escape into an open channel when L^\pm is less than R , since particles must travel a distance $> R$ before they reach the channel surface.

When the escape sphere cuts into the perpendicular wall (where the walls *parallel to the x-axis* will subsequently be referred to as ‘perpendicular’ walls),

$$d/2 - R_1 \leq Y < d/2, \quad (27)$$

the situation becomes more complicated. Here, a portion of the escape sphere will correspond to alpha or ${}^7\text{Li}$ particles emitted into the perpendicular MCP wall. Therefore, we must subtract Area 1 of the escape sphere from the hemisphere shown in Fig. 19. These particles, emitted into Areas 1 and 3, will not contribute at all to the neutron detection process. Emission into Area 2 corresponds to particles that exit the MCP channel wall and then strike the surface of the perpendicular wall, inducing an electron avalanche. We therefore need not subtract from the escape probability $P_2^{\alpha(0)}$, the total escape sphere area subtended within the perpendicular channel wall $S_{\text{wall},1}$. Area 1 of the escape sphere can be found by first calculating the combined areas 1 and 2 ($S_{\text{wall},1}$ or the surface subtended by the perpendicular wall and the plane $X = \pm W/2$ for left- and right-escaping particles), and then subtracting the Area 2 from the escape sphere, $-S_{\text{wall},2}$. The reason we first calculate the area of the combined portions is that Area 2 vanishes when the Y coordinate lies in the range $d/2 \leq Y \leq d/2 + W$; see Section C.1.2, below.

C.1.1 Area of the surface on the escape sphere $S_{\text{wall},1}$ subtended by a perpendicular MCP wall

The equation for the surface of a sphere with radius R is

$$(x - x_0)^2 + (y - y_0)^2 + (z - z_0)^2 = R^2 \quad (28)$$

Substituting variables $t = x - x_0$, $u = y - y_0$ and $v = z - z_0$, we move the center of the escape sphere into the (t,u,v) center of coordinates. The element of the surface of this sphere can thus be expressed as [18]

$$dS = \sqrt{\left\{ \left(\frac{\partial t}{\partial u} \right)^2 + \left(\frac{\partial t}{\partial v} \right)^2 + 1 \right\}} dudv \quad (29)$$

Deriving t from (28) and substituting in (29) we obtain

$$dS = \frac{R}{\sqrt{(R^2 - u^2 - v^2)}} dudv \quad (30)$$

The area of the escape sphere subtended by the perpendicular channel wall (i.e., the combined Areas 1 and 2 of Fig. 19) can be found by integrating (30) with a proper selection of integration limits (with u varying between u_0 and u_1 as in Fig. 19.b, and v varying between $-\sqrt{R^2 - L^2 - u^2}$ and $\sqrt{R^2 - L^2 - u^2}$):

$$S_{wall,1} = \iint dS = \int_{u_0}^{u_1} du \int_{-\sqrt{R^2 - L^2 - u^2}}^{\sqrt{R^2 - L^2 - u^2}} \frac{R}{\sqrt{(R^2 - u^2 - v^2)}} dv = \int_{u_0}^{u_1} 2R \arcsin \left(\frac{\sqrt{(R^2 - L^2 - u^2)}}{\sqrt{(R^2 - u^2)}} \right) du \quad (31)$$

where L is the distance from the sphere center to the channel wall defined by (23) (Fig. 19.b), and $r = \sqrt{R^2 - L^2}$ is the radius of the circle at the intersection of the plane $u=Const$ and the escape sphere. Integrating (31), we obtain

$$S_{wall,1} = 2R[H(u_1) - H(u_0)] \quad (32)$$

where

$$\begin{aligned}
H(u) = & u \arcsin\left(\sqrt{\frac{R^2 - L^2 - u^2}{R^2 - u^2}}\right) - L \arctan\left(\frac{u}{\sqrt{R^2 - L^2 - u^2}}\right) + \\
& \frac{R}{2} \arctan\left(\frac{Ru + R^2 - L^2}{L\sqrt{R^2 - L^2 - u^2}}\right) + \frac{R}{2} \arctan\left(\frac{Ru - R^2 + L^2}{L\sqrt{R^2 - L^2 - u^2}}\right)
\end{aligned} \tag{33}$$

for $u^2 < R^2 - L^2$, $L \neq 0$, and $R \neq L$, while for other parameters $H(u)$ is expressed by:

$$H(u) = \begin{cases} 0, u^2 > R^2 - L^2 \\ \frac{\pi}{2}(R-L)\frac{u}{|u|}, u^2 = R^2 - L^2 \\ \frac{\pi}{2}u, L = 0 \\ 0, R \leq L \end{cases} \tag{34}$$

Note that $H(u)=0$ for $R \leq L$, because here the escape sphere does not intersect the perpendicular channel wall at all.

The probability that an alpha particle is emitted into the combined Areas 1 and 2 of the escape sphere, for the region where Y lies in the range determined by (27), is

$$P_{wall,1}(X, Y) = \frac{S_{wall,1}(X, Y)}{4\pi R^2} = \frac{H(u_1) - H(u_0)}{2\pi R} \tag{35}$$

We now must determine the limits of integration u_0 and u_1 , which correspond to distances from the sphere center to the sides of the perpendicular wall along the Y -axis. If only one side of the perpendicular wall crosses the escape sphere (where $|u_0| > r$ or $|u_1| > r$), then the limits of integration should be set to the radius $r = \sqrt{R^2 - L^2}$.

It follows that

$$\begin{cases} u_0 = \min\left(r, \left|\frac{d}{2} - Y\right|\right) * \text{sign}\left(\frac{d}{2} - Y\right) \\ u_1 = \min\left(r, \left|\frac{d}{2} - Y + W\right|\right) * \text{sign}\left(\frac{d}{2} - Y + W\right) \end{cases} \quad (36)$$

C.1.2 Probability of alpha particle absorption in a perpendicular channel wall

As mentioned earlier, some alpha particles do escape into an open channel and also strike a perpendicular channel wall, thereby producing an electron avalanche. In the opposite case, where the alpha is unable to escape into a channel, because it is absorbed by a perpendicular channel wall (Area 1 on the escape surface of Fig. 19), we must subtract the surface area of Section 2 (Fig. 19) on the escape sphere $S_{\text{wall},2}$ (which exists only for Y in the range of (27)). Then, $S_{\text{wall},2}$ can be determined in the same manner as $S_{\text{wall},1}$, with the integration done within the range $u \in [u_0', u_1']$ and $v \in \left[-\sqrt{R^2 - u^2 / \sin^2(\beta)}, \sqrt{R^2 - u^2 / \sin^2(\beta)}\right]$:

$$S_{\text{wall},2}(X, Y) = \int_{u_0'}^{u_1'} du \int_{-\sqrt{R^2 - u^2 / \sin^2(\beta)}}^{\sqrt{R^2 - u^2 / \sin^2(\beta)}} \frac{R}{\sqrt{(R^2 - u^2 - v^2)}} dv = \int_{u_0'}^{u_1'} 2R \arcsin\left(\frac{\sqrt{R^2 - u^2 / \sin^2(\beta)}}{\sqrt{(R^2 - u^2)}}\right) du \quad (37)$$

So that

$$S_{\text{wall},2}(X, Y) = \begin{cases} 2R \left[G(u_1') - G(u_0') \right]; & u_1' * u_0' > 0 \\ 0; & u_1' * u_0' \leq 0 \end{cases} \quad (38)$$

Similar to the limits of integration u_0 and u_1 in (36), u_0' and u_1' are determined by the following equation:

$$\begin{cases} u_0' = \min\left(|R \sin(\beta)|, \left|\frac{d}{2} - Y\right|\right) * \text{sign}\left(\frac{d}{2} - Y\right) \\ u_1' = \min\left(|R \sin(\beta)|, \left|\frac{d}{2} - Y + W\right|\right) * \text{sign}\left(\frac{d}{2} - Y + W\right) \end{cases} \quad (39)$$

where

$$\sin(\beta) = \min(|u_0|, |u_1|) * \text{sign}(u_0) / \sqrt{[\min(|u_0|, |u_1|)]^2 + L^2} \quad (40)$$

It is to be noted from (36) that u_0 and u_1 are nonzero and have the same sign. $G(u)$ in (38)

is obtained by integrating (37):

$$\begin{aligned} G(u) = & u \arcsin\left(\sqrt{\frac{R^2 - u^2/\sin^2(\beta)}{R^2 - u^2}}\right) + \\ & \frac{R}{2} \arctan\left(\frac{(u - R \sin^2(\beta)) * \text{sign}(u)}{\sqrt{R^2 \sin^2(\beta) - u^2} \sqrt{\cos^2(\beta)}}\right) - \frac{R}{2} \arctan\left(\frac{(u + R \sin^2(\beta)) * \text{sign}(u)}{\sqrt{R^2 \sin^2(\beta) - u^2} \sqrt{\cos^2(\beta)}}\right) \end{aligned} \quad (41)$$

for the cases u and L nonzero and not equal to $R \sin(\beta)$, L nonzero, and $R > L$, while for other parameters $G(u)$ is expressed by:

$$G(u) = \begin{cases} 0, u = R \sin(\beta) \\ 0, u = 0 \\ \frac{\pi}{2} u, L = 0 \\ 0, R \leq L \end{cases} \quad (42)$$

Finally we calculate the probability of emission into Area 2 of the escape sphere:

$$P_{\text{wall},2}(X, Y) = \frac{S_{\text{wall},2}(X, Y)}{4\pi R^2} \quad (43)$$

Thus for Y in the range of (27) the probability that an alpha particle is emitted into a channel is

$$P_2^\alpha(X, Y) = P_2^{\alpha(0)}(X, Y) - \left(P_{wall,1}(X, Y) - P_{wall,2}(X, Y) \right) \Big|_{L(X)=L^+, R=R1} - \left(P_{wall,1}(X, Y) - P_{wall,2}(X, Y) \right) \Big|_{L(X)=L^-, R=R1} \quad (44)$$

Note that escape to both sides of the channel wall (at distance L^+ and L^- from the point of neutron capture) is taken into account in (44).

For Y values in the range

$$d/2 \leq Y \leq d/2 + W \quad (45)$$

the escape probability P_2^α can still be calculated from (44), since Area 2 of the escape sphere (Fig. 20) vanishes (i.e, from (38) $P_{wall,2} = 0$ as u_0 becomes negative).

C.2 ${}^7\text{Li}$ escape probability $P_2^{\text{Li}}(X, Y)$ when alpha is absorbed within the MCP channel wall

As discussed above, only those ${}^7\text{Li}$ particles emitted diametrically to its paired alpha particle that is entirely absorbed within an MCP channel wall are considered in total detection efficiency calculations. If the alpha is emitted nominally to the right as viewed from the point of neutron reaction, then the associated ${}^7\text{Li}$ particle is emitted nominally to the left (and vice versa - unless they both are emitted parallel to the plane $X = \text{Const}$, and both particles are contained within the wall). As before in the case of the alpha escape probability, we start with the simplest case $P_2^{\text{Li}(0)}$ (the total escape probability of ${}^7\text{Li}$ into an MCP channel), when a neutron is absorbed far from the corner of a channel with Y in the range as in (22), $0 \leq Y < d/2 - R_1$

$$P_2^{\text{Li}(0)}(X, Y) \equiv P_2^{\text{Li}(0)}(X) = \frac{1}{4\pi R_2^2} [S_{Li,0}^+(X) + S_{Li,0}^-(X)], \quad (46)$$

where $S_{Li,0}$ represents the combined areas 2 and 3 of Fig. 21:

$$S_{Li,0}^{\pm}(X) = F(L^{\pm}(X), R_2) \quad (47)$$

We now subtract those ${}^7\text{Li}$ particles corresponding to alphas emitted into an open channel. Fig. 21 shows schematically Area 2 ($S_{Li,1}$) on the escape sphere, which has to be subtracted from $S_{Li,0}$ (the combined areas 2 and 3). The only ${}^7\text{Li}$ particles contributing to the total detection efficiency will be those emitted into angles corresponding to Area 3 on the escape sphere (assuming such an area exists, as it depends on the W, R_1, R_2 and X parameters in Fig. 21.b-d). The area of the surface 2, $-S_{Li,1}$, which is to be subtracted from $S_{Li,0}$, can be found from:

$$S_{Li,1}^+(X) = \begin{cases} F1^+(X), & X > 0 \\ S_{Li,0}^+, & X \leq 0 \end{cases} \quad S_{Li,1}^-(X) = \begin{cases} F1^-(X), & X < 0 \\ S_{Li,0}^-, & X \geq 0 \end{cases}$$

where

$$F1(X)^{\pm} = \begin{cases} 0; & R_1 \leq \frac{W}{2} \\ 0; & \text{abs}(X) \geq R_1 - \frac{W}{2}, R_1 > \frac{W}{2} \\ F(L^{\pm}, R_2); & R_1 + R_2 > W, \text{abs}(X) \leq \frac{W}{2} \frac{R_1 - R_2}{R_1 + R_2} \\ F(L^{\pm}, R_2); & R_1 + R_2 \leq W, R_1 > \frac{W}{2}, \text{abs}(X) \leq R_1 - \frac{W}{2} \\ F\left(\frac{R_2}{R_1} L^{\mp}, R_2\right); & \frac{W}{2} \frac{R_1 - R_2}{R_1 + R_2} < \text{abs}(X) < R_1 - \frac{W}{2} \end{cases}$$

When a neutron is absorbed far from the channel corner, this absorption can result in both alpha and ${}^7\text{Li}$ particles escaping into a channel. However, both of those particles correspond to only a single neutron event. The probability of ${}^7\text{Li}$ particles not contributing to the neutron detection event, is

$$P_2^{Li(1)}(X, Y) \equiv P_2^{Li(1)}(X) = \frac{1}{4\pi R_2^2} [S_{Li,1}^+(X) + S_{Li,1}^-(X)] \quad (48)$$

and the probability of ${}^7\text{Li}$ contributing to the unique detection event is then determined by

$$P_2^{Li}(X, Y) = P_2^{Li(0)}(X) - P_2^{Li(1)}(X) - P_2^{Li(2)}(X, Y) + P_2^{Li(3)}(X, Y) \quad (49)$$

The two new terms introduced in equation (49) take into account the case of particle absorption in the perpendicular MCP wall: $P_2^{Li(2)}$ is the probability of a Li particle being absorbed in the perpendicular MCP wall, and $P_2^{Li(3)}$ is the probability of Li escaping into the open channel, with the corresponding recoil alpha particle being totally absorbed by the perpendicular channel wall.

C.2.1 Probability $P_2^{Li(2)}$ of ${}^7\text{Li}$ absorption in a perpendicular channel wall

If a neutron is absorbed close to the channel corner, certain ${}^7\text{Li}$ particles will be entirely absorbed inside the MCP perpendicular walls (similar to case of alpha absorption discussed in Section C.1.2). Here, the calculation is complicated by the fact that we have to subtract only those Li particles absorbed in the wall, which were not taken into account in $P_2^{Li(1)}$. Therefore, we first calculate the probability of ${}^7\text{Li}$ particle emission into the perpendicular wall, but with a new escape range R_2 :

$$P_{wall}^{Li(1)}(X, Y) = \left(P_{wall,1}(X, Y) - P_{wall,2}(X, Y) \right) \Big|_{L(X)=L^+, R=R_2} + \left(P_{wall,1}(X, Y) - P_{wall,2}(X, Y) \right) \Big|_{L(X)=L^-, R=R_2} \quad (50)$$

Some of the ${}^7\text{Li}$ particles emitted into the perpendicular wall were already accounted for as ‘non-escaping’ particles in the previous section ($S_{Li,1}$ in (48) as well as the corresponding surface Area 2 in Fig. 21). We reduce $P_{wall}^{Li(1)}$ by subtracting those particles already accounted for in (50), shown as Area 1 in Fig. 22.

$$P_{wall}^{Li(2)}(X, Y) = (F_{wall}^{Li}(X, Y))^+ + (F_{wall}^{Li}(X, Y))^-$$

where $F_{wall}^{Li}(X, Y)^\pm = \left(P_{wall,1}(X, Y)^\pm - P_{wall,2}(X, Y)^\pm \right)_{L^\pm(X)=L^\pm, W^\pm=(W')^\pm, d^\pm=(d')^\pm, R=R_2}$

$P_{wall,1}(X, Y)$ is calculated by combining (33)-(36), and $P_{wall,2}(X, Y)$ is calculated from (38)-(43). For $P_{wall,1}(X, Y)$, we set $u_0^\pm \equiv u_0(R_2, L^\pm)$ and $u_1^\pm \equiv u_1(R_2, L^\pm)$, and for $P_{wall,2}(X, Y)$ we replace d, R, W and L by d', R_2, W' and L' ;

$$L'^\pm = \min \left(\max \left(L^\pm \frac{R_2}{R_1}, L^\pm \right), R_2 \right)$$

$$d'^\pm = \begin{cases} d + 2u_1 \left(1 - \frac{L'^\pm}{L^\pm} \right); & u_0 < 0, u_1 < 0 \\ d + 2u_0 \left(\frac{L'^\pm}{L^\pm} - 1 \right); & u_0 > 0, u_1 > 0 \\ d; & u_0 * u_1 \leq 0 \end{cases} \quad (51)$$

$$W'^\pm = \begin{cases} u_1 \frac{L'^\pm}{L^\pm} - \max \left(u_0, -\sqrt{R_2^2 - (L'^\pm)^2} \right); & u_0 < 0, u_1 < 0 \\ \min \left(u_1, \sqrt{R_2^2 - (L'^\pm)^2} \right) - u_0 \frac{L'^\pm}{L^\pm}; & u_0 > 0, u_1 > 0 \\ W_2; & u_0 * u_1 \leq 0 \end{cases} \quad (52)$$

Finally, the probability that Li particles are emitted into the perpendicular channel wall but are not taken into account in $P_2^{Li(l)}$ is

$$P_2^{Li(2)}(X, Y) = \left(P_{wall}^{Li(1)}(X, Y) - P_{wall}^{Li(2)}(X, Y) \right) \quad (53)$$

**C.2.2 The probability $P_2^{Li(3)}$ of ${}^7\text{Li}$ escaping into the channel,
with the corresponding alpha particle being entirely absorbed
in a perpendicular MCP wall**

In previous sections we eliminated recoil ${}^7\text{Li}$ particles that correspond to the alpha particles emitted into an open channel, $P_2^{Li(1)}$ (with none of the alpha particles emitted into the perpendicular wall). We then continued calculating the probability that the ${}^7\text{Li}$ particle itself is absorbed by the perpendicular MCP wall, $P_2^{Li(2)}$. We now have to correct $P_2^{Li(1)}$ for those recoil ${}^7\text{Li}$ particles that are emitted into a channel but with the corresponding alpha particles absorbed entirely by the perpendicular channel wall (Area 3 in Fig. 23). As in previous sections, we take into account emission both to the left and right:

$$P_2^{Li(3)}(X, Y) = (G_{He-wall}^{Li}(X, Y))^+ + (G_{He-wall}^{Li}(X, Y))^-$$

We first calculate u_0 and u_1 from (36), for either L^+ or L^- and $R=R_1$; $u_0^\pm \equiv u_0(R_1, L^\pm)$; $u_1^\pm \equiv u_1(R_1, L^\pm)$. (For the remainder of this section, u_0 and u_1 denote the values calculated from (36) using L^\pm and R_1 .) There are two possible combinations of the parameters X , Y , d and W leading to different equations for calculation of $G_{\alpha-wall}^{Li}(X, Y)$.

The first is:

- 1) $u_0^\pm(R_1, L^\pm) * u_1^\pm(R_1, L^\pm) > 0$, as in Fig. 23a,b:

$$G_{\alpha-wall}^{Li}(X, Y)^\pm = (P_{wall,1}(X, Y) - P_{wall,2}(X, Y)) \Big|_{d=(d^\pm), W=(W^\pm), L=(L^\pm), R=R_2}$$

where both $P_{wall,1}$ and $P_{wall,2}$ are calculated from (33)-(35) and (38)-(43), respectively, with the parameters d, L, R and W changed to d'', L'', R_2 and W'' . L'' is found from (56), d'' , and W'' using the following:

$$d^{\pm''} = d - 2 \left[\min \left(|u_0(R_1, L^{\mp})|, |u_1(R_1, L^{\mp})| \right) \left(1 - \frac{L^{\pm''}}{L^{\mp}} \right) \right] \quad (54)$$

$$W^{\pm''} = \frac{L^{\pm''}}{L^{\mp}} |u_0(R_1, L^{\mp}) - u_1(R_1, L^{\mp})| \quad (55)$$

The second combination is:

2) $u_0^{\pm}(R_1, L^{\pm}) * u_1^{\pm}(R_1, L^{\pm}) \leq 0$, as in Fig. 23c:

$$G_{\alpha-wall}^{Li}(X, Y)^{\pm} = P_{wall,1}(X, Y) \Big|_{u_0=(u_0'')^{\pm}, u_1=(u_1'')^{\pm}, L=(L'')^{\pm}, R=R_2},$$

where $P_{wall,1}$ is calculated from (33)-(35) with u_0 and u_1 changed to u_0'' and u_1'' , L changed to L'' and R equal to R_2 . Next, L'' , u_0'' and u_1'' are calculated from the following:

$$L^{\pm''} = \min \left(\max \left(L^{\mp} \frac{R_2}{R_1}, L^{\pm} \right), R_2 \right) \quad (56)$$

$$u_0^{\pm''} = \begin{cases} \min \left(\sqrt{R_2^2 - L^{\mp''}}, |u_0^{\mp}| \right); & u_0^{\mp} + u_1^{\mp} > 0, u_0^{\mp} * u_1^{\mp} \leq 0 \\ \min \left(\sqrt{R_2^2 - L^{\mp''}}, |u_1^{\mp}| \right); & u_0^{\mp} + u_1^{\mp} < 0, u_0^{\mp} * u_1^{\mp} \leq 0 \end{cases} \quad (57)$$

$$u_1^{\pm''} = \begin{cases} \min \left(\sqrt{R_2^2 - L^{\mp''}}, \max \left[|u_0^{\mp}|, \frac{u_1^{\mp} R_2}{R_1} \right] \right); & u_0^{\mp} + u_1^{\mp} > 0, u_0^{\mp} * u_1^{\mp} \leq 0 \\ \min \left(\sqrt{R_2^2 - L^{\mp''}}, \max \left[\frac{|u_0^{\mp}| R_2}{R_1}, |u_1^{\mp}| \right] \right); & u_0^{\mp} + u_1^{\mp} < 0, u_0^{\mp} * u_1^{\mp} \leq 0 \end{cases} \quad (58)$$

References

- [1] G.W. Fraser, J.F. Pearson, "The direct detection of thermal-neutrons by imaging microchannel-plate detectors", Nucl. Instr. Meth. A **293** (1990) pp.569-574.
- [2] G.W.Fraser, J.F. Pearson, W.B. Feller, L.M. Cook, O.S. Al-Horayess, "Thermal neutron imaging using microchannel plates", Proc. SPIE Vol. **1737** (1992) 298.
- [3] W.B. Feller, R.G. Downing, P.L. White, "Neutron field imaging with microchannel plates", Proc. SPIE Vol. **4141**, Hard X-Ray, Gamma-Ray, and Neutron Detector Physics II, Ralph B. James; Richard C. Schirato; Eds. (2000) pp.291-302.
- [4] K. Wien, O. Becker, P. Daab and D. Nederveld , "Experimental investigation of fission fragment and alpha-recoil induced ejection of secondary ions", Nucl. Instr. Meth. **170** (1980) pp. 477-481.
- [5] J. L Wiza, "Microchannel plate detectors", Nucl. Instr. Meth. **162** (1979) pp. 587-601.
- [6] O.H.W. Siegmund, A.S. Tremsin, J.V. Vallerga and J. Hull, "Cross strip imaging anodes for microchannel plate detectors", IEEE Trans. Nucl. Sci. **48** pp.430-434 (2001).
- [7] A.S. Tremsin, O.H.W. Siegmund, J.V. Vallerga, J. Hull, R. Abiad, "Cross Strip Readouts for Photon Counting Detectors with High Spatial and Temporal Resolution ", to appear in IEEE Trans. Nucl. Sci.
- [8] H.C. Straub, M.A. Mangan, B.G. Lindsay, K.A. Smith, and R.F. Stebbings, "Absolute detection efficiency of a microchannel plate detector for kilo-electron volt energy ions", Rev. Sci. Instr. **70** (1999) pp.4238-4240.
- [9] G.W. Fraser, "The ion detection efficiency of microchannel plates (MCPs)", International Journal of Mass Spectrometry **215** (2002) pp.13–30
- [10]J.J. Fijol, A.M. Then, G.W. Tasker, et. al., "Secondary-Electron yield of SiO₂ and Si₃N₄ thin-films for continuous dynode electron multipliers", Appl. Surf. Sci. **48** (1991) pp.464-471.
- [11]K. Takahashi, S. Tazaki, J. Miyahara, Y. Karasawa, N. Niimura, "Imaging performance of imaging plate neutron detectors, Nucl. Instr. Meth. A **377** (1996) pp.119-122.
- [12]G.W. Fraser, X-ray Detectors in Astronomy, Cambridge University Press, 1989.
- [13]G.F. Knoll, "Radiation Detection and Measurement", Third Edition, Wiley, 2000.
- [14]P.M. Shikhaliev, "Hard X-ray detection model for microchannel plate detectors", Nucl. Instr. Meth. A **398** (1997) pp. 229-37.

- [15] available for download from the web site: <http://www.srim.org/srim/SRIMINTRO.htm>.
- [16] B.N. Laprade, R C. Cochran, F. Langevin, M.W. Dykstra, "Characterization of an ultrasmall-pore microchannel plate" in Ultrahigh- and High-Speed Photography and Image-based Motion Measurement, D.R. Snyder; A. Davidhazy; T. Etoh; C.B. Johnson, J. S. Walton; Eds., *Proc. SPIE* **3173** (1997) pp. 474-485.
- [17] A.S. Tremsin, D.F.R. Mildner, W.B. Feller, R.G. Downing, "Very Compact High Performance Microchannel Plate Neutron Collimators", to appear in *IEEE Trans. Nucl. Sci.*
- [18] G.A. Korn, T.M.Korn, "Mathematical handbook for scientists and engineers", McGraw-Hill book company, Inc, New York 1961, Section 5.4.6.

5. Figure captions

Fig. 1 Schematic of neutron detection within a boron-doped MCP structure.

Fig. 2. Comparison of circular-, hexagonal- and square-pore geometry for neutron detecting MCP. If neutron absorption is within area **1**, the products of the reaction will escape into MCP pore and start an electron avalanche (detected neutron); area **2** corresponds to the case when reaction products get reabsorbed within the MCP wall –and the neutron is not detected.

Fig. 3. Schematic diagram of "stacked" thermal neutron detector. A neutron capture reaction takes place in ^{10}B doped MCP converter positioned above standard MCP stack (MCP-amplifier). The output charge cloud is collected by a readout element that is transparent to neutrons (grid, cross delay line anode made of the necessary materials, etc.). The operating voltage of the detector does not increase with the number of MCP stacks.

Fig. 4. Averaging the escape probability P_2 over the neutron capture positions (X, Y) within the MCP wall. The averaging described by equation 5 is done separately for regions I (P_2^I) and II (P_2^{II})

Fig. 5. Calculated length of single neutron path within the MCP glass walls as a function of incidence angle θ for three different azimuths φ . $d = 8 \mu\text{m}$, $W = 2\mu\text{m}$, $L_{\text{MCP}} = 1000 \mu\text{m}$, neutron energy 0.025 eV ($\sigma(^{10}\text{B})=3837$ barns), MCP glass has 10 mol percent of ^{10}B , MCP glass density 3.86 g cm^{-3} . The neutron incidence position is in the middle of MCP wall $(x_0, y_0)=(W/2, W/2)$, see Fig. 17.

Fig. 6. Averaged probability P_1 of neutron absorption within the MCP glass as a function of incidence angle θ for different azimuths φ . Averaging is over possible positions (x_0, y_0) of the neutron incidence on the MCP surface. All parameters are the same as in Fig. 5.

Fig. 7. Averaged probability P_1 of neutron absorption within the MCP glass as a function of incidence angles θ and φ . Averaging is over possible positions (x_0, y_0) of neutron incidence on the MCP surface. All

parameters are the same as in Fig. 5. **(a)** no correction for the $\sim\sin(\theta)$ area loss (the MCP is assumed to be much larger than the neutron beam width). **(b)** corrected for the area loss.

Fig. 8. Averaged probability P_1 of neutron absorption within the MCP glass as a function of incidence angles θ and φ . No correction for the area loss (the MCP is assumed to be much larger than the neutron beam width). Averaging is over possible positions (x_0, y_0) of neutron incidence on the MCP surface. All parameters are the same as in Fig. 5, except the MCP thickness L_{MCP} is 3000 μm .

Fig. 9. Probability of escape into an MCP pore for ^4He ($P_2^\alpha(X=Const, Y)$, solid line), only ^7Li in MCP pore with ^4He absorbed in the MCP glass ($P_2^{Li}(X=Const, Y)$, dotted line) and the probability of at least one particle to escape into MCP pore ($P_2(X=Const, Y)$, dash - dotted line). MCP pore width is $d = 8 \mu\text{m}$, wall thickness $W = 2 \mu\text{m}$. The escape ranges of ^4He and ^7Li particles are $R_1 = 3.5 \mu\text{m}$ and $R_2 = 2 \mu\text{m}$, respectively. **(a)** $X = 0 \mu\text{m}$ - center of the wall, escape probabilities are the smallest. **(b)** $X = 0.5 \mu\text{m}$. **(c)** $X = 0.75 \mu\text{m}$. $Y = 4 \mu\text{m}$ corresponds to the corner of the MCP pore; $Y = 5 \mu\text{m}$ corresponds to the middle of crossing between the MCP glass walls, where the escape probability is minimal for both particles. Closer to the wall surface is the neutron capture point (X, Y) , the larger are the escape probabilities.

Fig. 10. Probability of ^4He escape into MCP pore $P_2^\alpha(X, Y)$ as a function of neutron absorption point (X, Y) for the MCP with pore width $d = 8 \mu\text{m}$ and the wall thickness $W = 2 \mu\text{m}$. The insert shows the area inside the MCP wall for which the probability was calculated.

Fig. 11. Probability of ^7Li escape into MCP pore $P_2^{Li}(X, Y)$ with the recoil ^4He being absorbed in the MCP glass. Parameters are the same as in Fig. 10.

Fig. 12. Probability of at least one particle to escape into MCP pore - $P_2(X, Y)$. **(a)** MCP pore width is $d = 8 \mu\text{m}$, wall thickness $W = 2 \mu\text{m}$. **(b)** the MCP pore width is $d = 16 \mu\text{m}$, the wall thickness $W = 4 \mu\text{m}$. The probability $P_2(X, Y)$ reaches unity when the neutron is absorbed close to the MCP wall surface and it drops to its minimum within crossing of the MCP walls.

Fig. 13. The averaged probability of ^4He escape into MCP pore $\langle P_2^\alpha(X,Y) \rangle$ as a function of the MCP pore width d and wall thickness W . Averaging is done over all possible coordinates of neutron absorption (X,Y) according to (5) (see also Fig. 4).

Fig. 14. The averaged probability of ^7Li escape into MCP pore $\langle P_2^{\text{Li}}(X,Y) \rangle$ as a function of the MCP pore width d and wall thickness W . Averaging is done over all possible coordinates of neutron absorption (X,Y) , eq. 5, Fig. 4.

Fig. 15. The averaged probability of at least one particle to escape into MCP pore - $\langle P_2(X,Y) \rangle$ **(a)** as a function of the MCP pore width d and wall thickness W . **(b)** as a function of the MCP pore width d for a fixed MCP wall thickness W . Contribution of only ^7Li particles to the total probability is also shown. Averaging is done over all possible coordinates of neutron absorption (X,Y) , eq. 5, Fig. 4.

Fig. 16. Schematic diagram of neutron capture in boron-doped MCP and system of coordinates used for calculation of absorption probability P_1 .

Fig. 17. 2-D projection of neutron path in a microchannel plate with the wall thickness W and the pore width d .

Fig. 18. The escape hemispheres corresponding to ^4He emission to the right MCP pore and ^7Li recoil emission to the left pore. **^4He hemisphere:** **1** - area on the escape sphere, corresponding to absorption of ^4He inside the MCP wall, parallel to y -axis. **2** - particles escaping into an MCP pore and contributing to the detection process. **3** - particles absorbed in the wall, parallel to x -axis. **4** - particles, which are emitted into an MCP pore and then strike the x -axis wall, contributing to the detection process. **^7Li hemisphere:** **5** - ^7Li particles emitted into an MCP pore, corresponding to ^4He particles also emitted into an MCP pore (not contributing to neutron detection). **6** - particles, which are emitted into an MCP pore and then strike the x -axis wall, contributing to the detection process. **7** - particles absorbed in the wall, parallel to x -axis. **8** - recoil ^7Li particles corresponding to ^4He absorbed in the x -axis wall. These ^7Li contribute to the detection process. **9**- particles escaping into an MCP pore and contributing to the detection process.

Fig. 19. (a) Escape hemisphere for Y positions corresponding to (27). (b) 2-D projection of the escape sphere. **1** - area on the escape sphere, corresponding to absorption of ${}^4\text{He}$ inside the "perpendicular" (parallel to x-axis) MCP wall. **2** - particles emitted into an MCP pore and then strike the x-axis wall, contributing to the detection process. **2** - particles absorbed by the MCP wall parallel to y-axis.

Fig. 20. (a) Escape hemisphere for Y-positions corresponding to (45). (b) 2-D projection of the escape sphere. **1** - area on the escape sphere, corresponding to absorption of ${}^4\text{He}$ inside the "perpendicular" (parallel to x-axis) MCP wall.

Fig. 21. (a) Escape hemispheres for ${}^4\text{He}$ (right) and ${}^7\text{Li}$ (left) for Y-positions corresponding to (27). (b)-(d) 2-D projection of the escape spheres. (b) All ${}^7\text{Li}$ particles add to the escape probability P_2 as none of them correspond to recoil ${}^4\text{He}$ escaped into an MCP pore. (c) $L^+ > L^-$: some Li add up to the detection efficiency. (d) $L^+ < L^-$: All ${}^7\text{Li}$ particles correspond to ${}^4\text{He}$ escaped into an MCP pore already: none of ${}^7\text{Li}$ add to the escape probability P_2 . **1** - ${}^4\text{He}$ particles are emitted into an MCP pore. **2** - ${}^7\text{Li}$ particles that already have recoil ${}^4\text{He}$ in the opposite MCP pore - not adding to the probability P_2 . **3** - ${}^7\text{Li}$ particles emitted into an MCP pore while their corresponding ${}^4\text{He}$ are absorbed within the wall glass should be counted as separate detection events adding to the probability P_2 .

Fig. 22. Correction for Li particles emitted into the perpendicular wall, which were already subtracted in (48) and (49) as surface area 2 of Fig. 21 (or combined surfaces 1 and 2 in this figure). (a), (b) ${}^4\text{He}$ escaping to the right and ${}^7\text{Li}$ to the left for Y positions corresponding to (27). (c) Y positions corresponding to condition (45). **1** - ${}^7\text{Li}$ particles emitted into the perpendicular wall, which were already subtracted as the ones already having recoil ${}^4\text{He}$ in the MCP pore and to be added back as $F_{wall}^{Li}(X, Y)^-$. **2** - ${}^7\text{Li}$ particles, which already have recoil ${}^4\text{He}$ in the opposite MCP pore - not adding to the probability P_2 .

Fig. 23. Correction for recoil Li particles corresponding to He particles emitted into the perpendicular MCP wall. Particles in area 3 have been eliminated from the detection process in (48) and (49) as surface area 2 of Fig. 21 and have to be added back as $P_2^{Li(3)}$. (a), (b) ${}^4\text{He}$ escaping to the right and ${}^7\text{Li}$ to the left for Y positions corresponding to (27). (c) Y positions corresponding to condition (45) **1** - ${}^4\text{He}$ particles absorbed in the perpendicular wall. **2** - ${}^4\text{He}$ particles, which are emitted into the MCP pore and then strike the x-axis

wall, contributing to the detection process. $3 - {}^7\text{Li}$ particles in the MCP pore, with the corresponding recoil ${}^4\text{He}$ absorbed in the "perpendicular" MCP wall, to be added back as $P_2^{Li(3)}$.

Fig.1

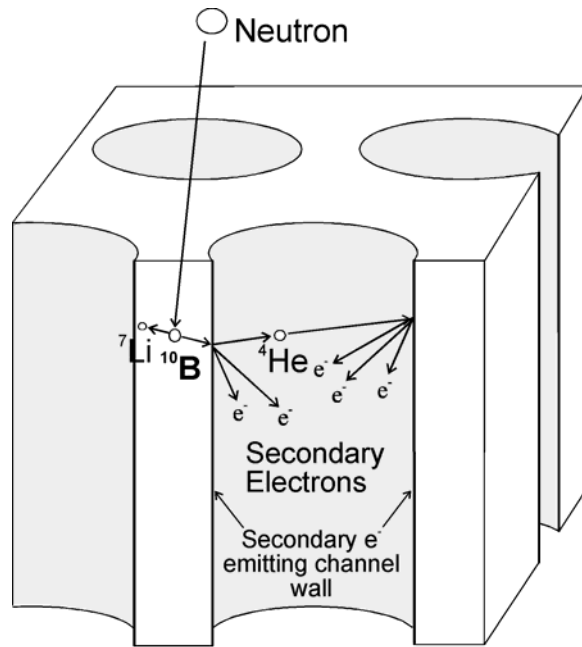
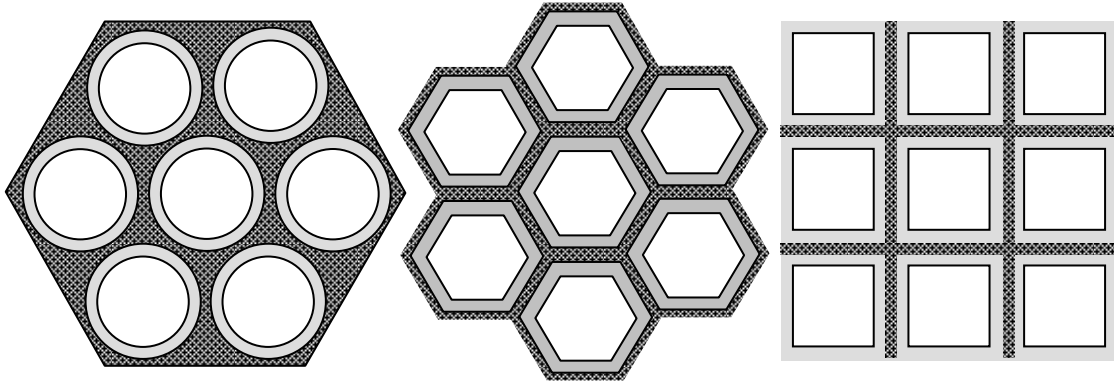


Fig. 2




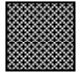
1 -  2 - 

Fig. 3

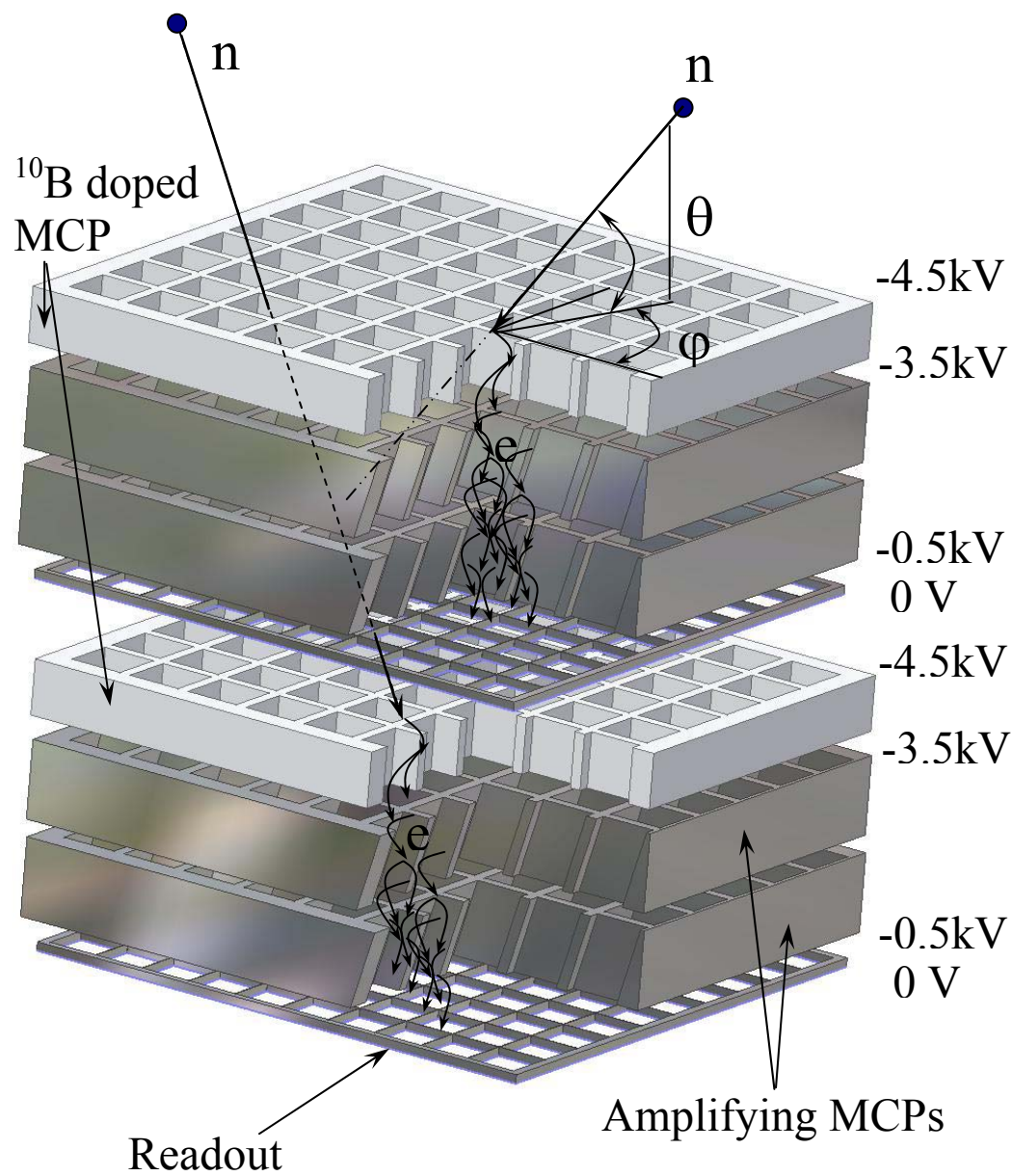


Fig. 4

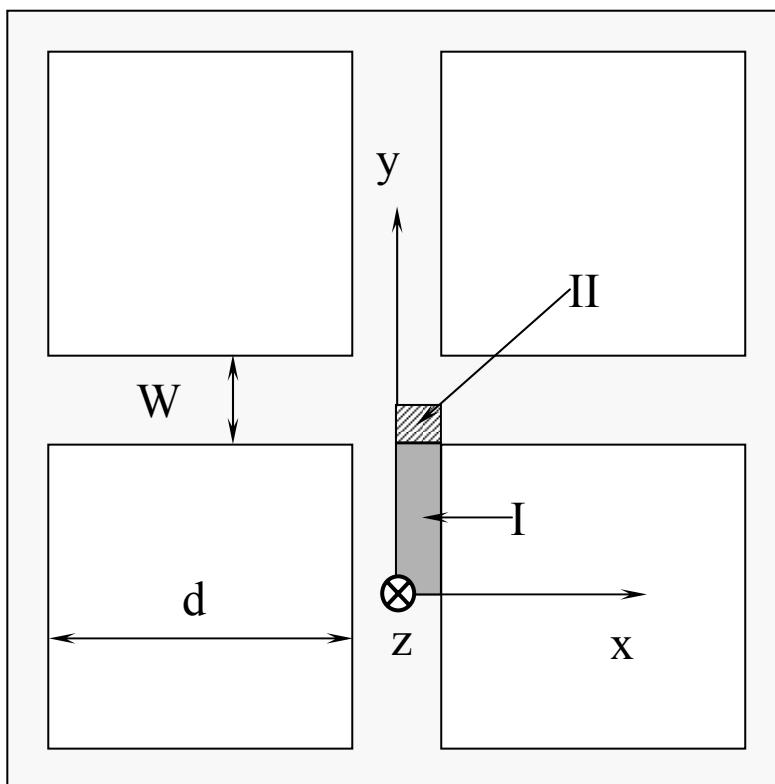


Fig. 5

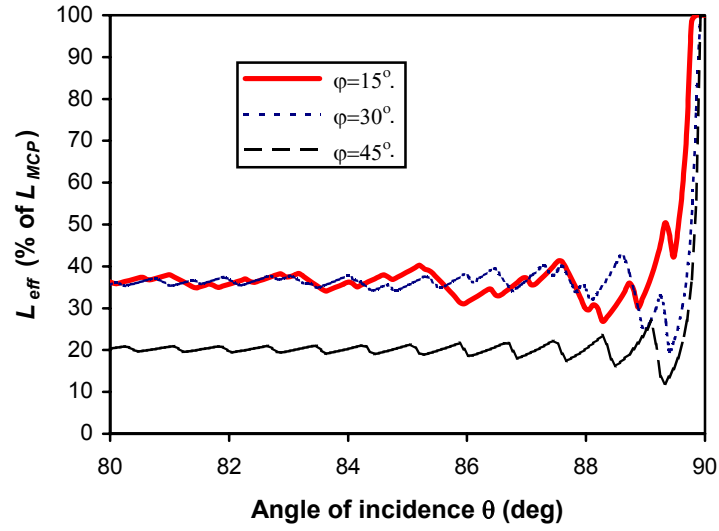


Fig. 6

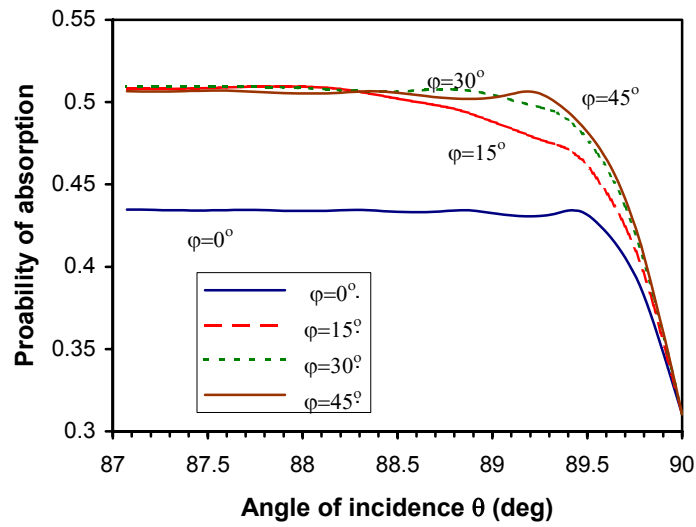


Fig. 7.a

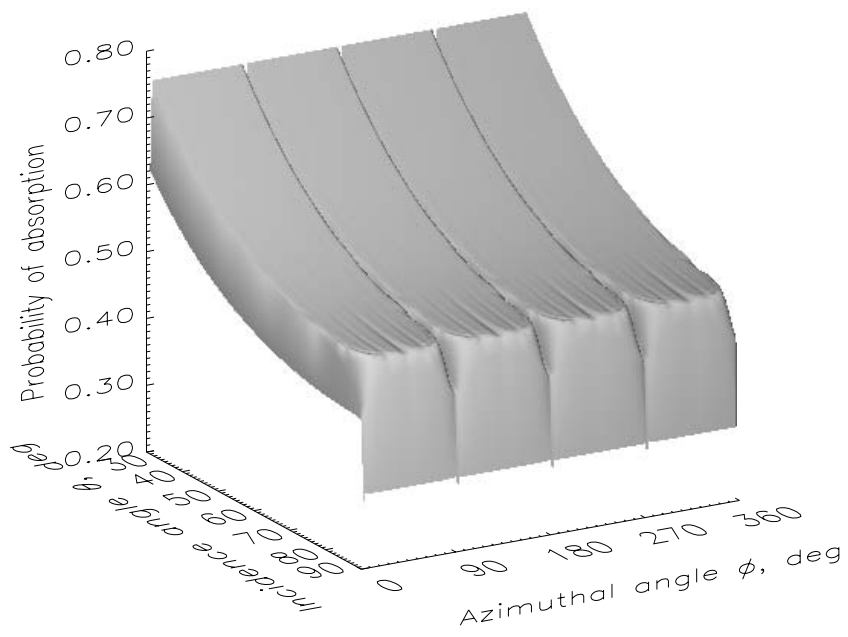


Fig. 7.b

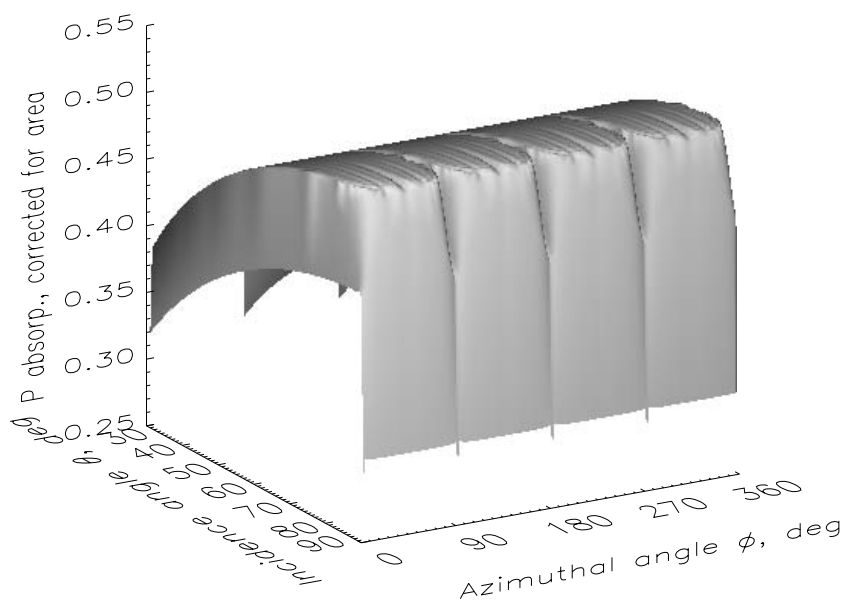


Fig. 8

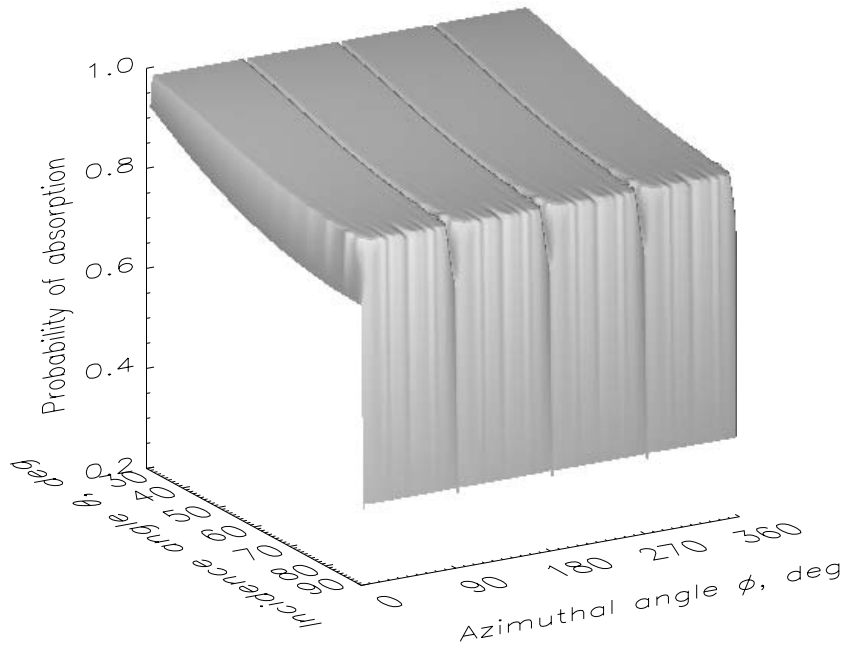


Fig. 9

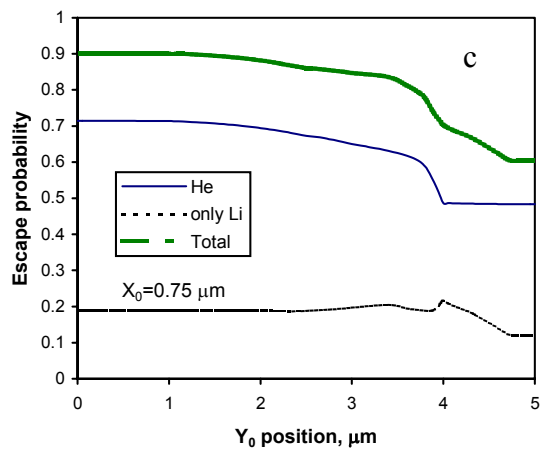
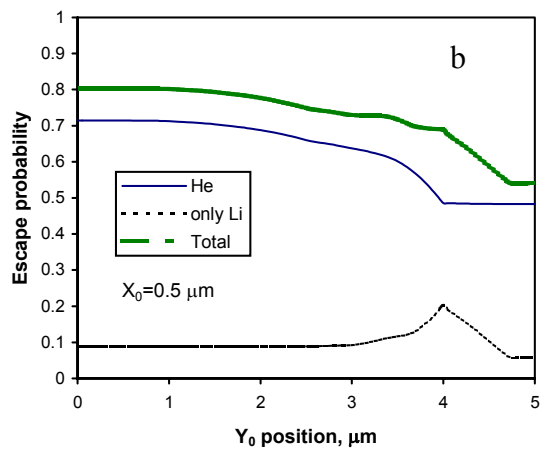
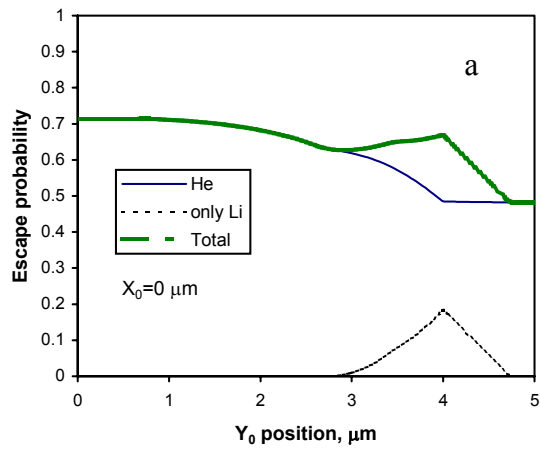


Fig. 10

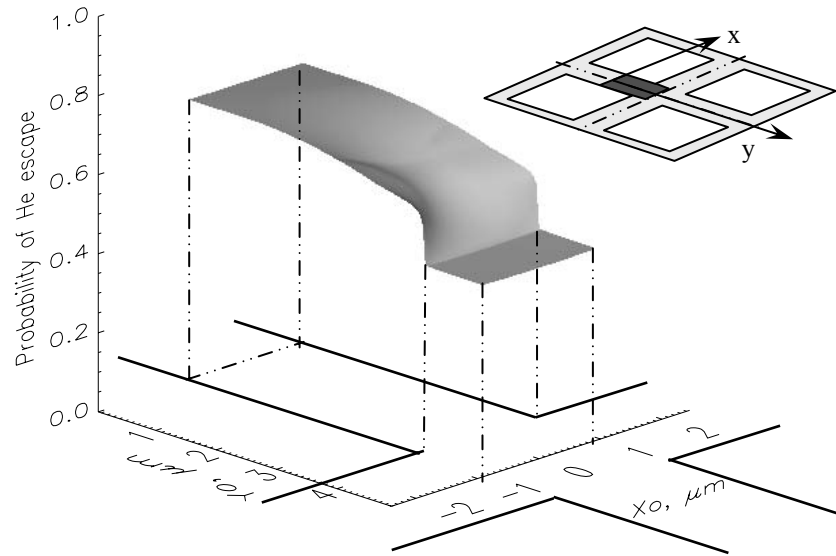


Fig. 11

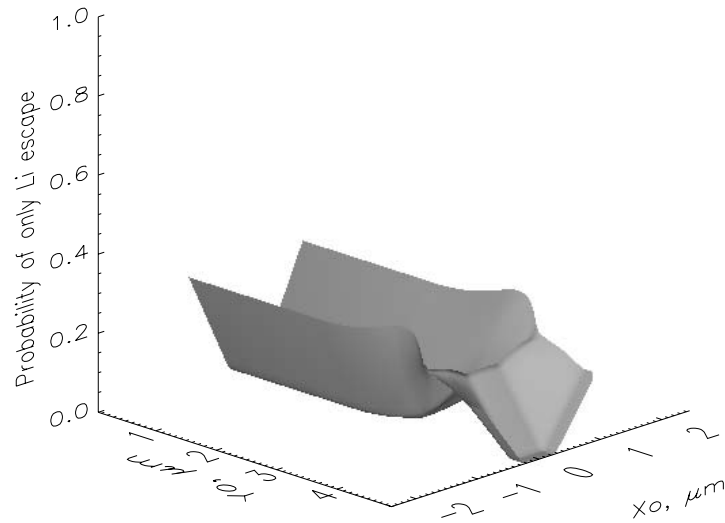


Fig. 12.a

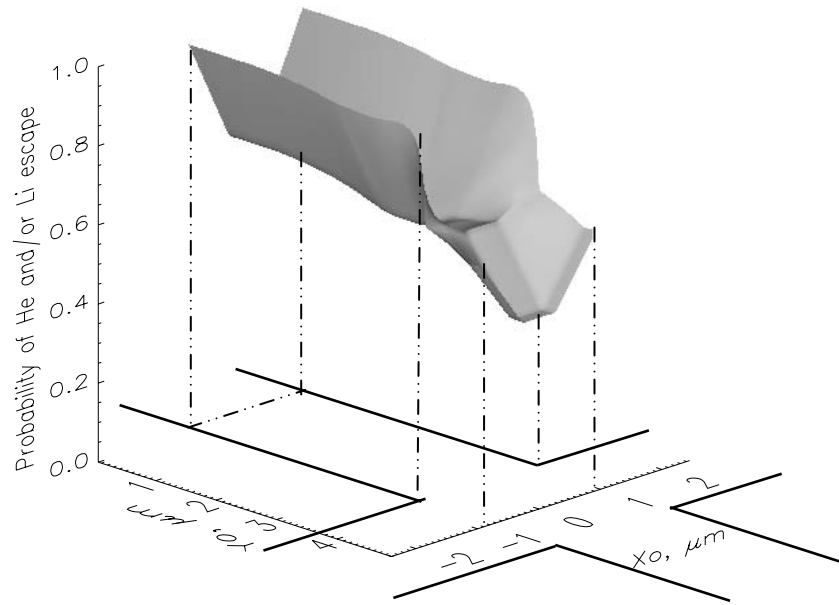


Fig. 12.b

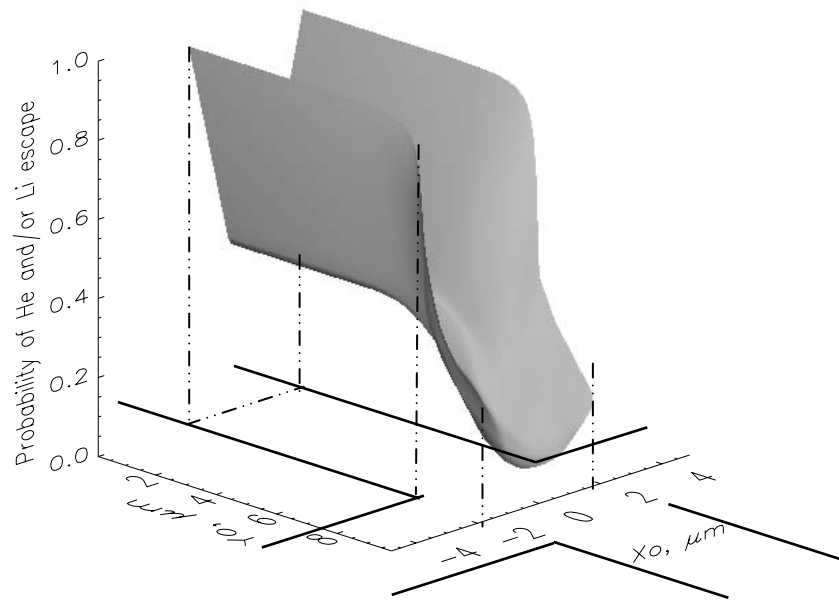


Fig. 13

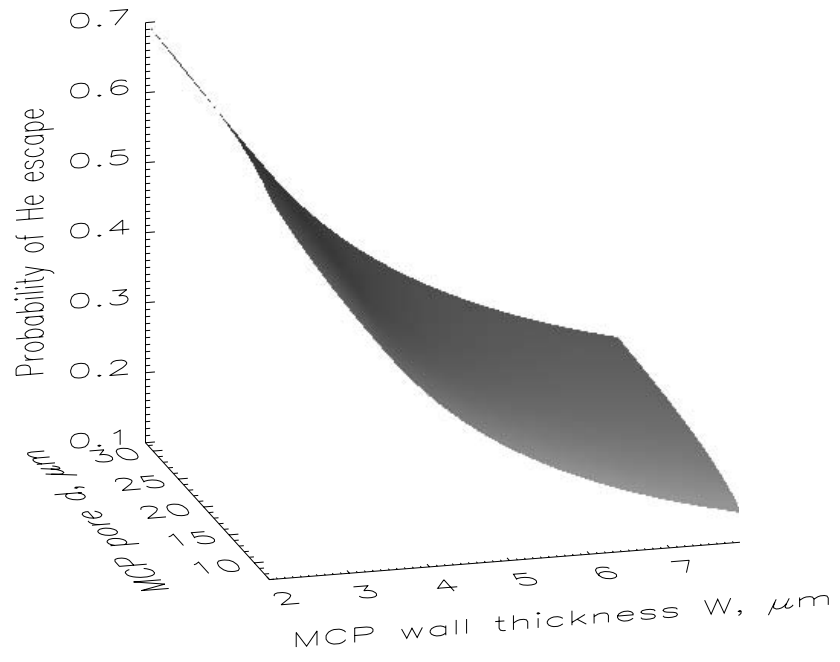


Fig. 14

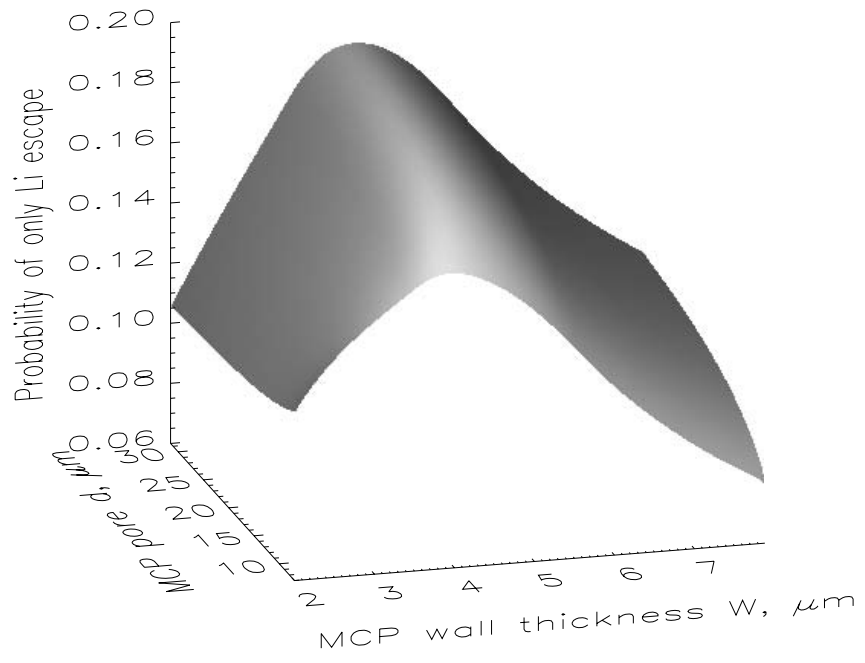


Fig. 15.a

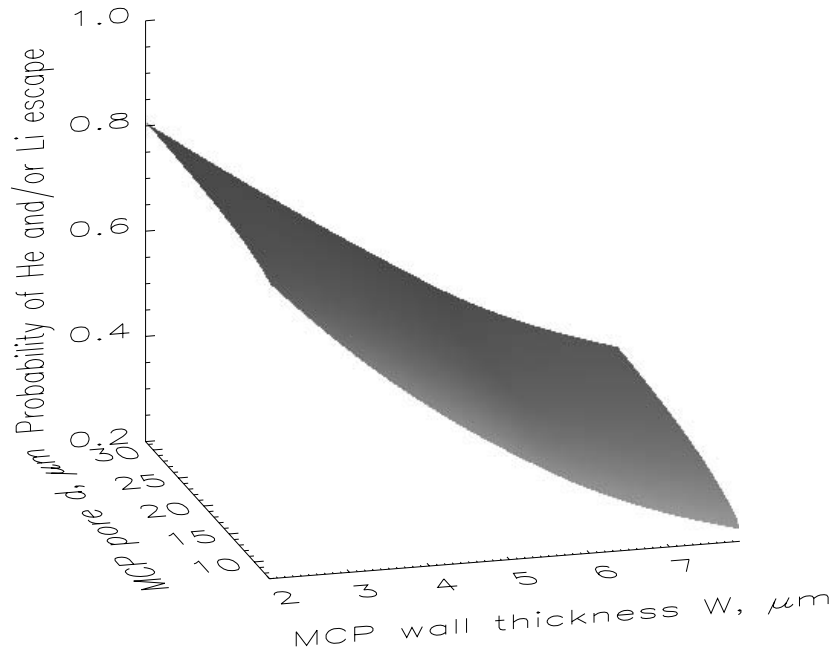


Fig. 15.b

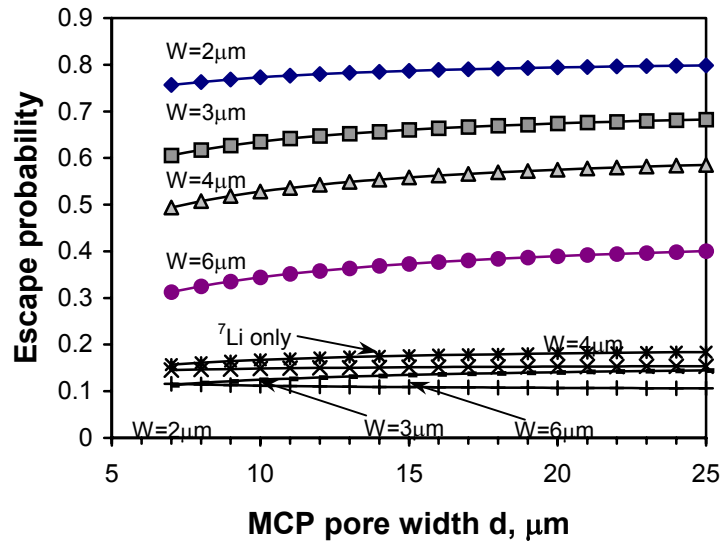


Fig. 16

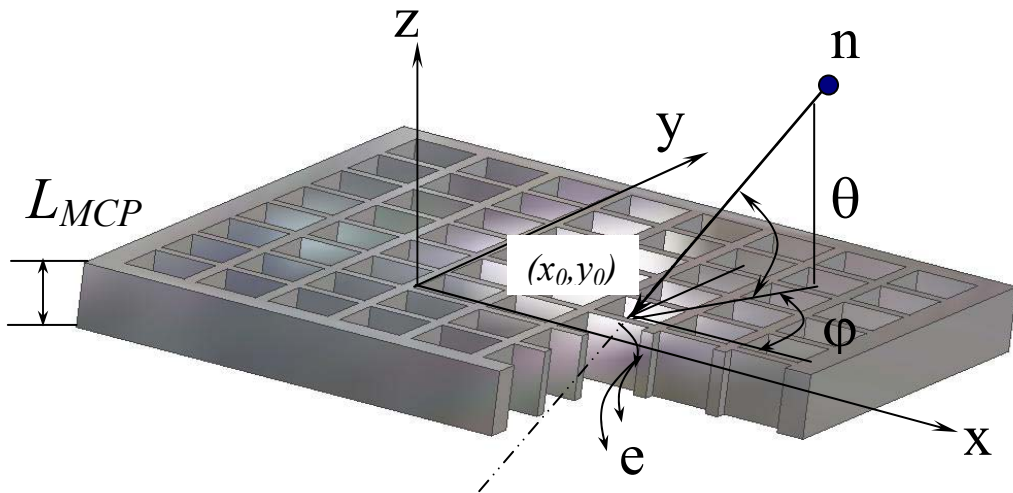


Fig. 17

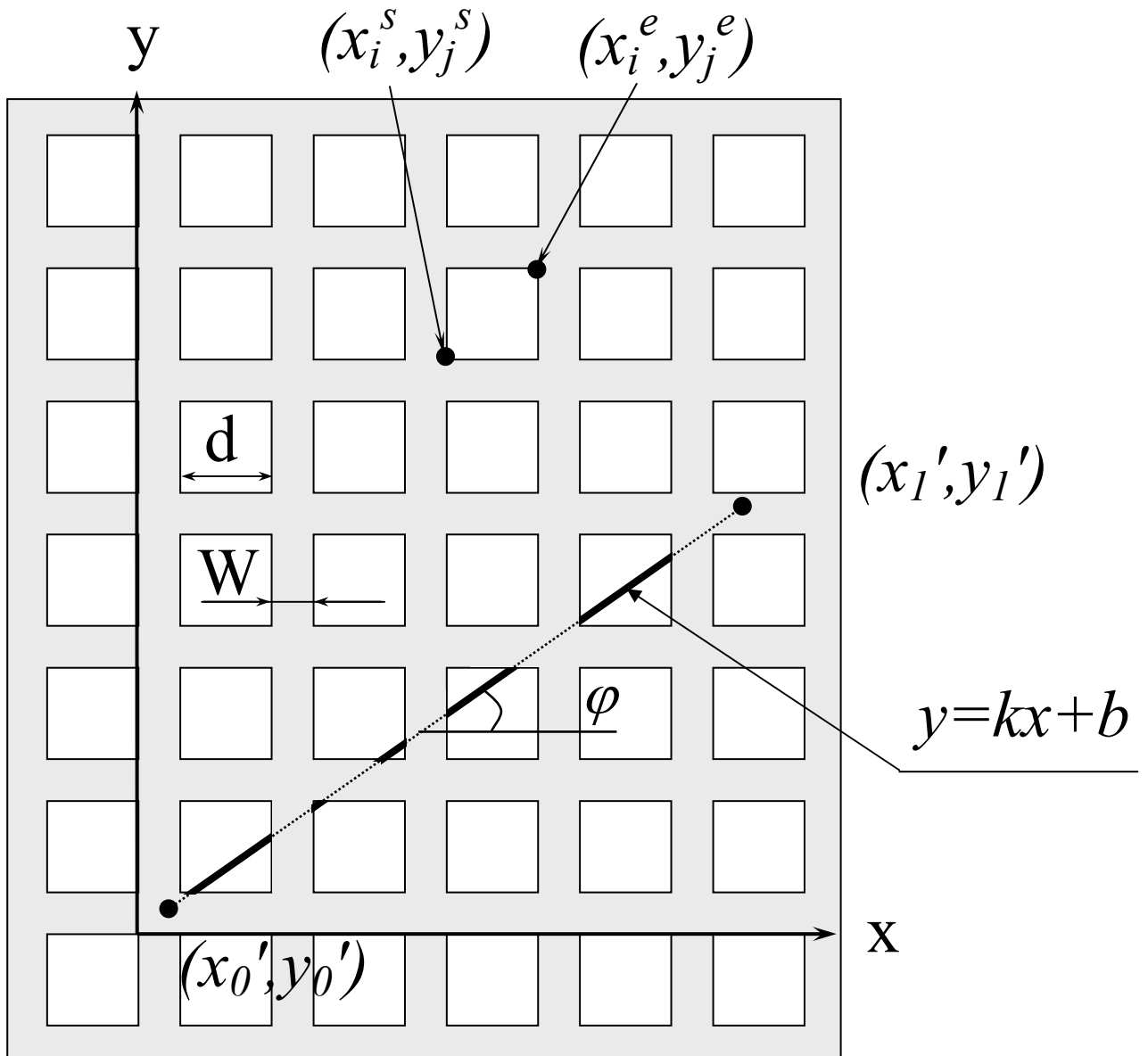


Fig. 18

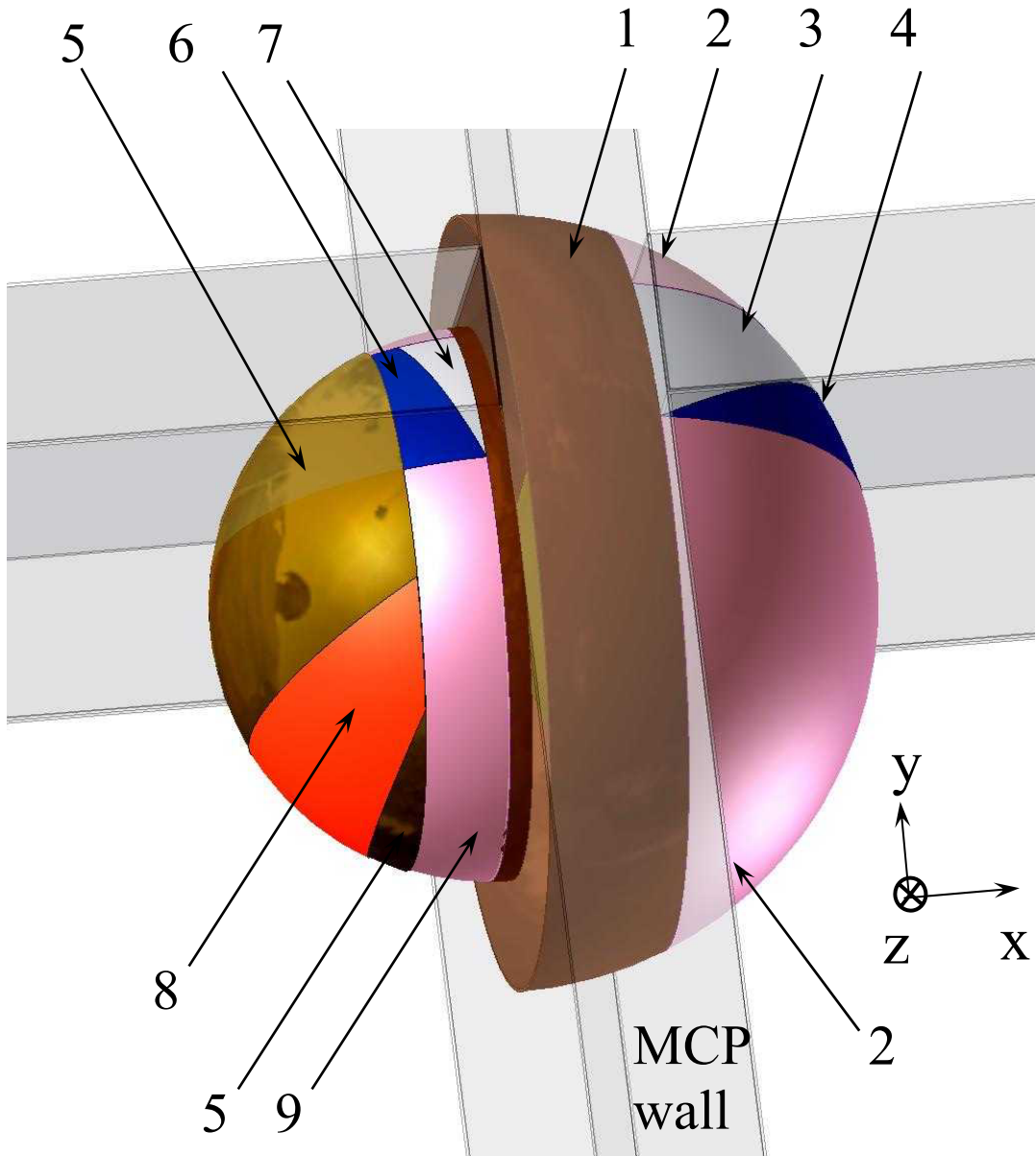


Fig. 19.a

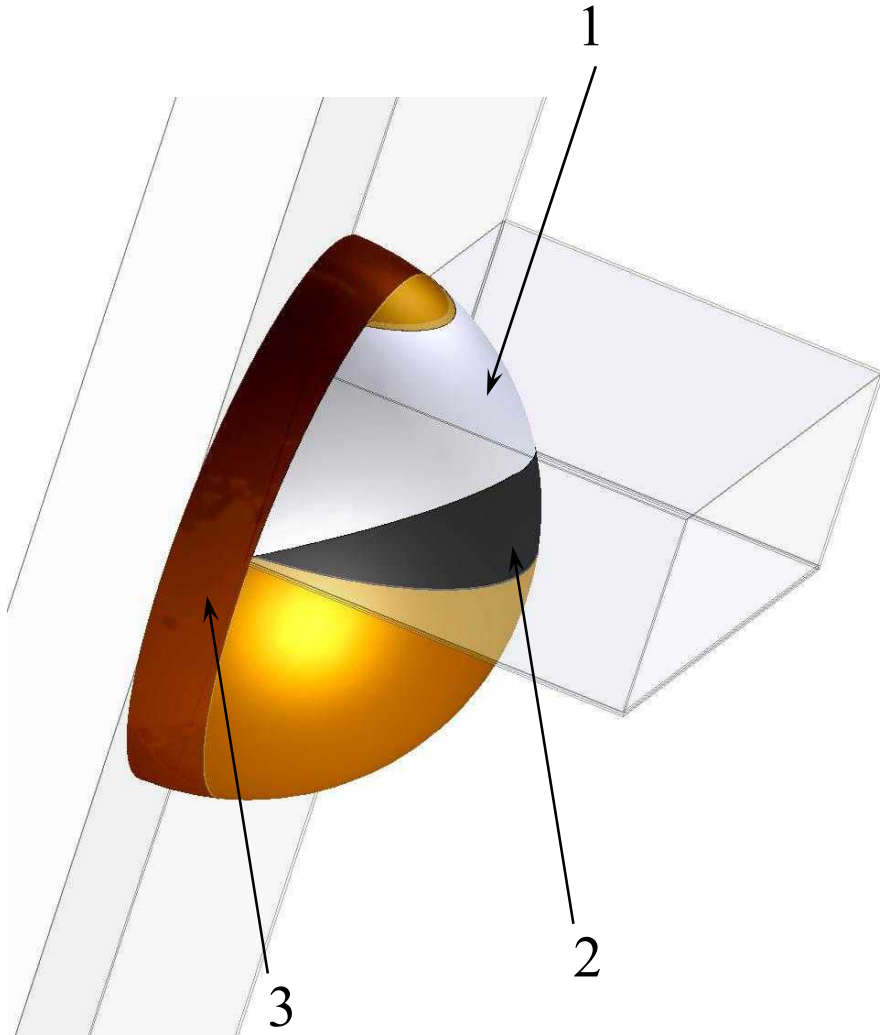


Fig. 19.b

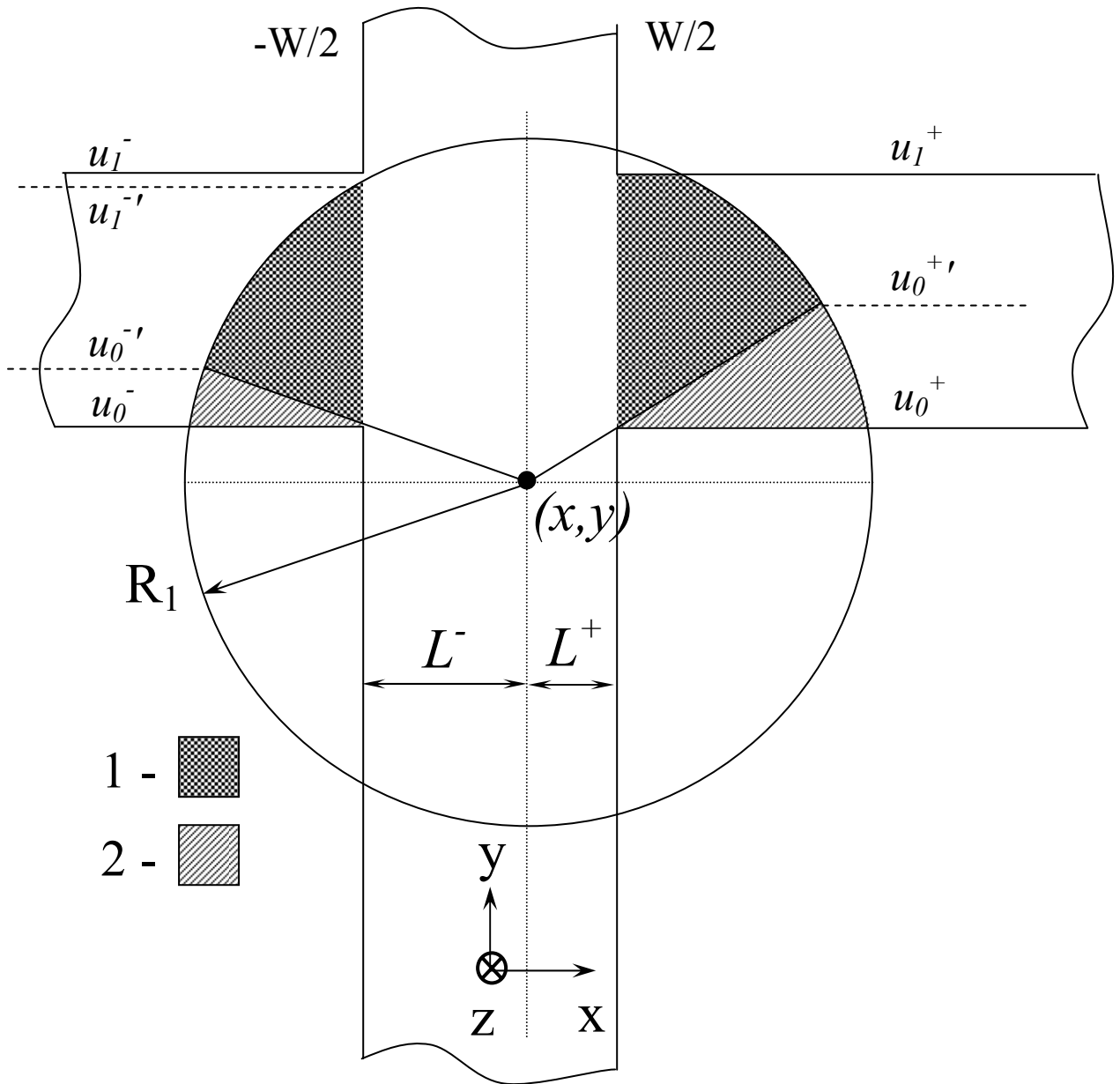


Fig. 20.a

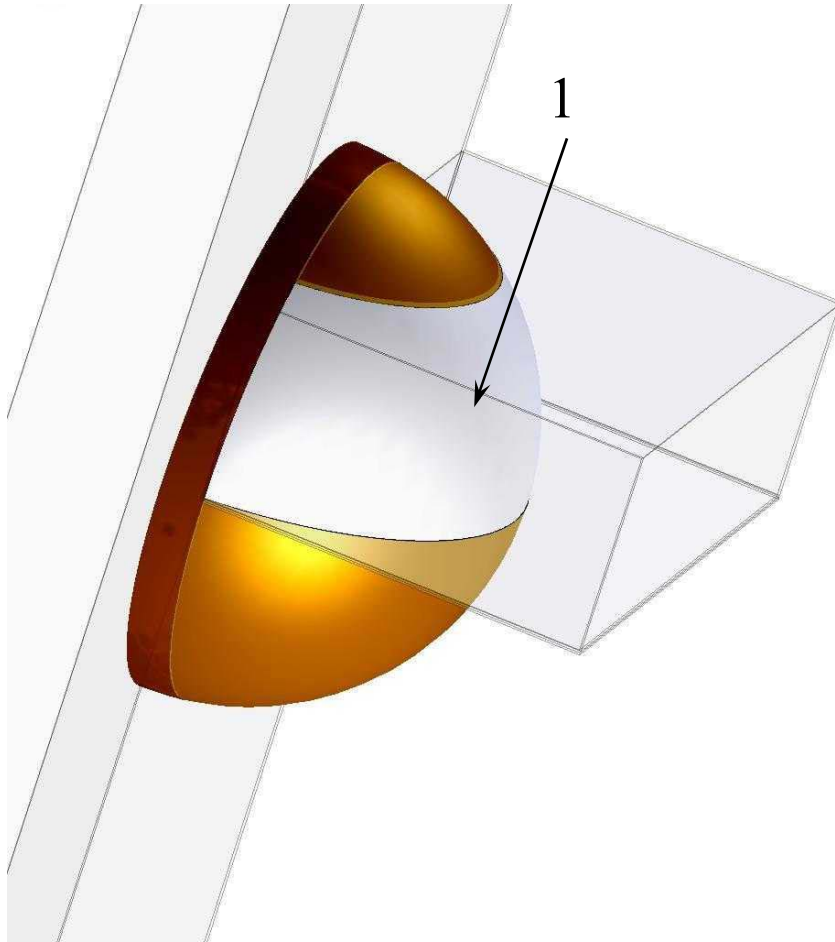


Fig. 20.b

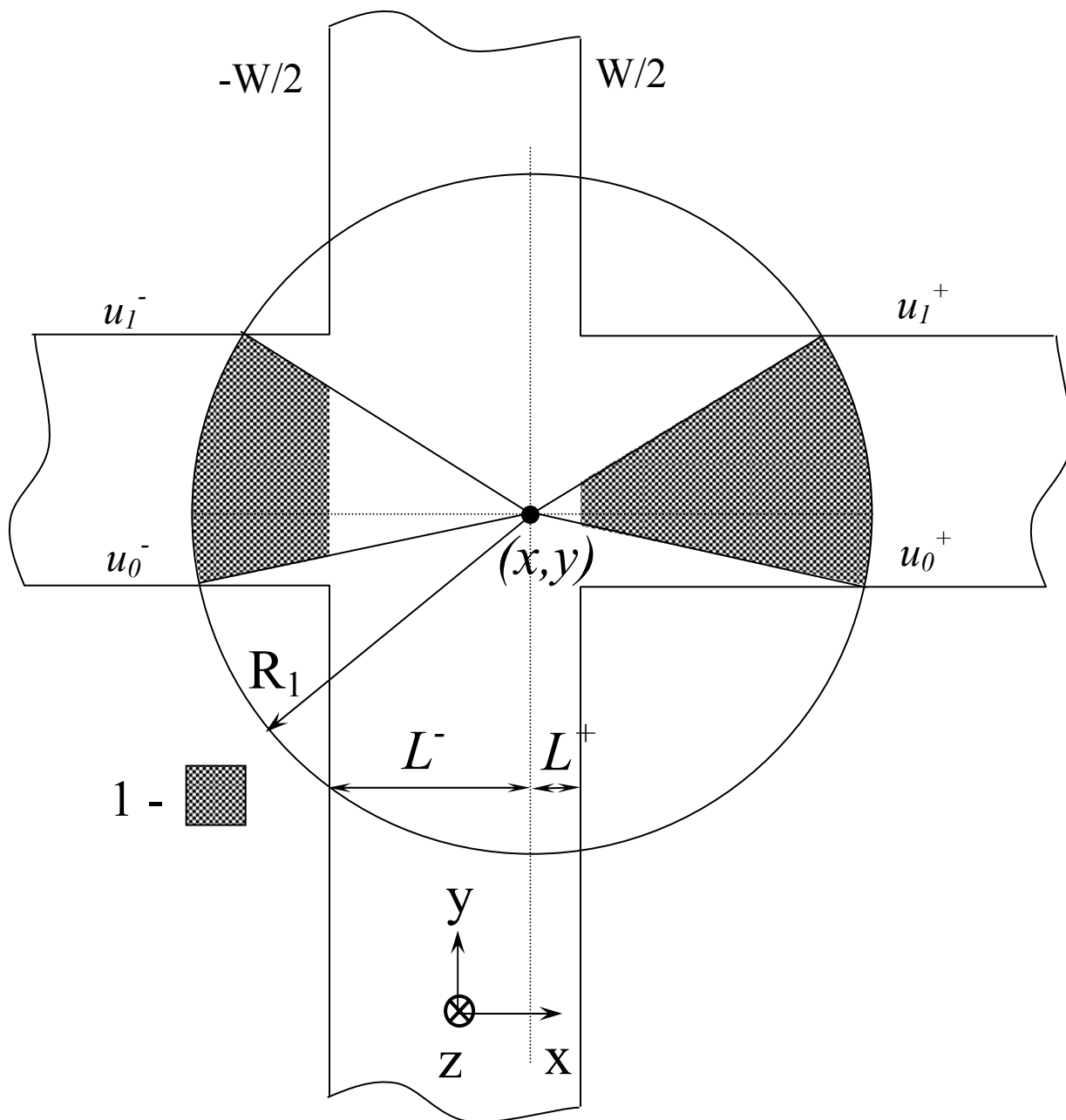


Fig. 21.a

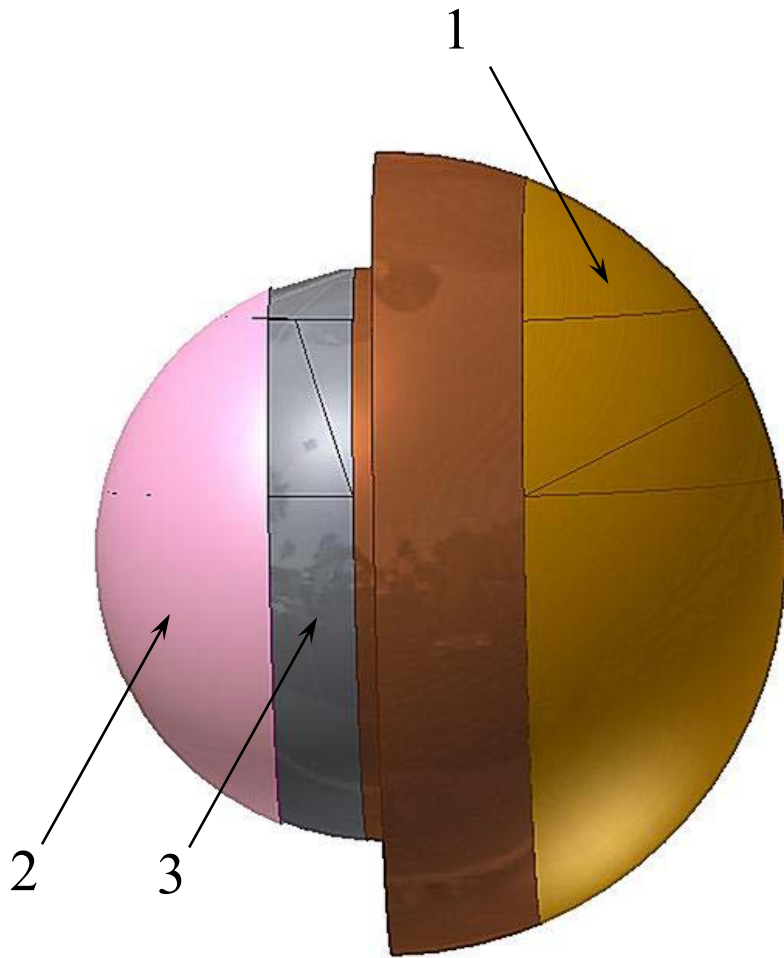


Fig. 21.b

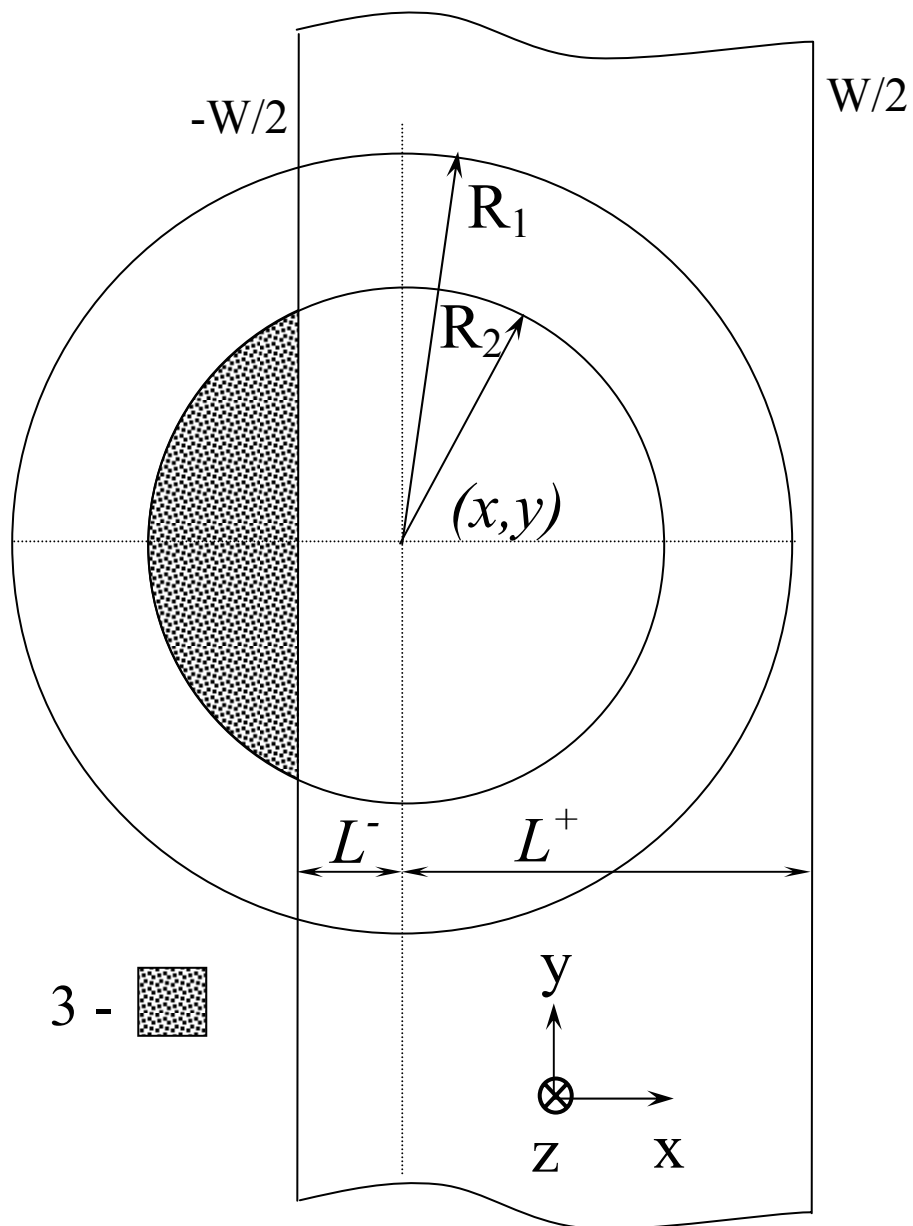


Fig. 21.c

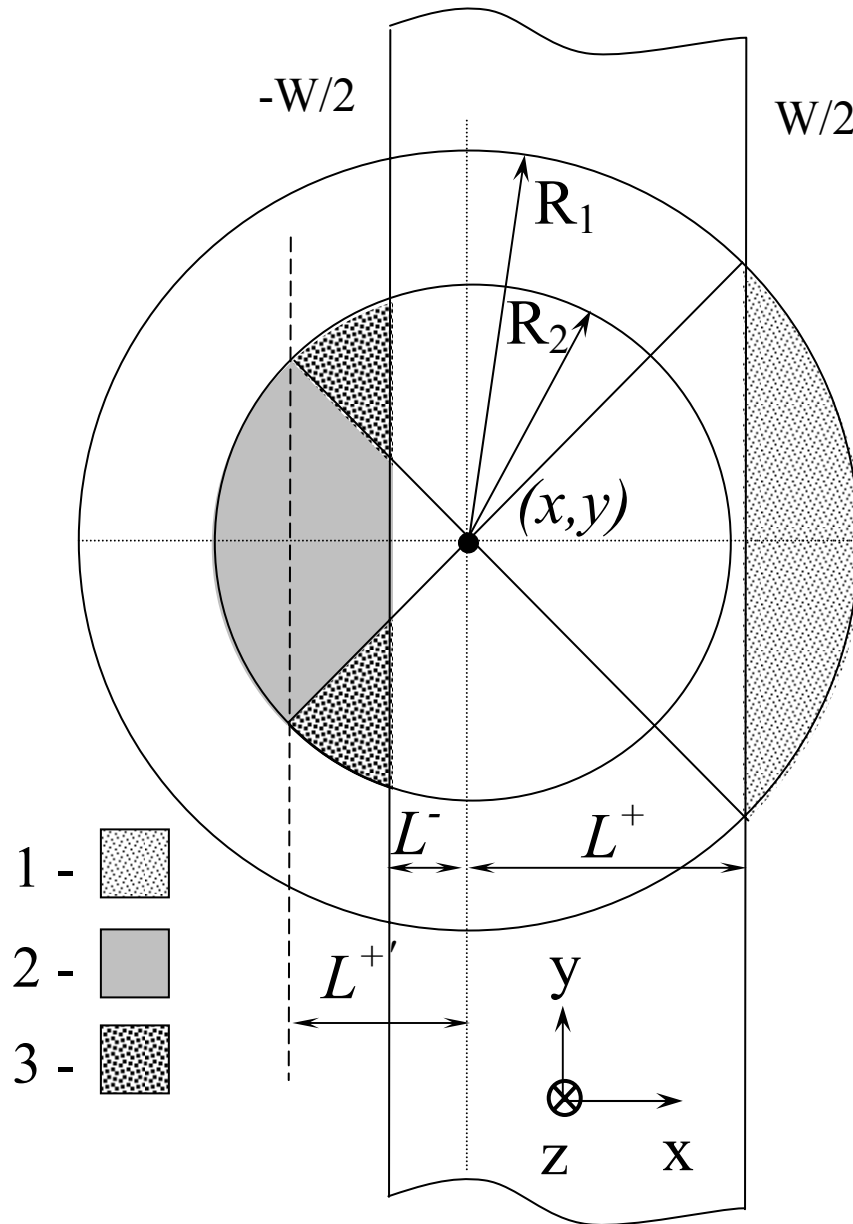


Fig. 21.d

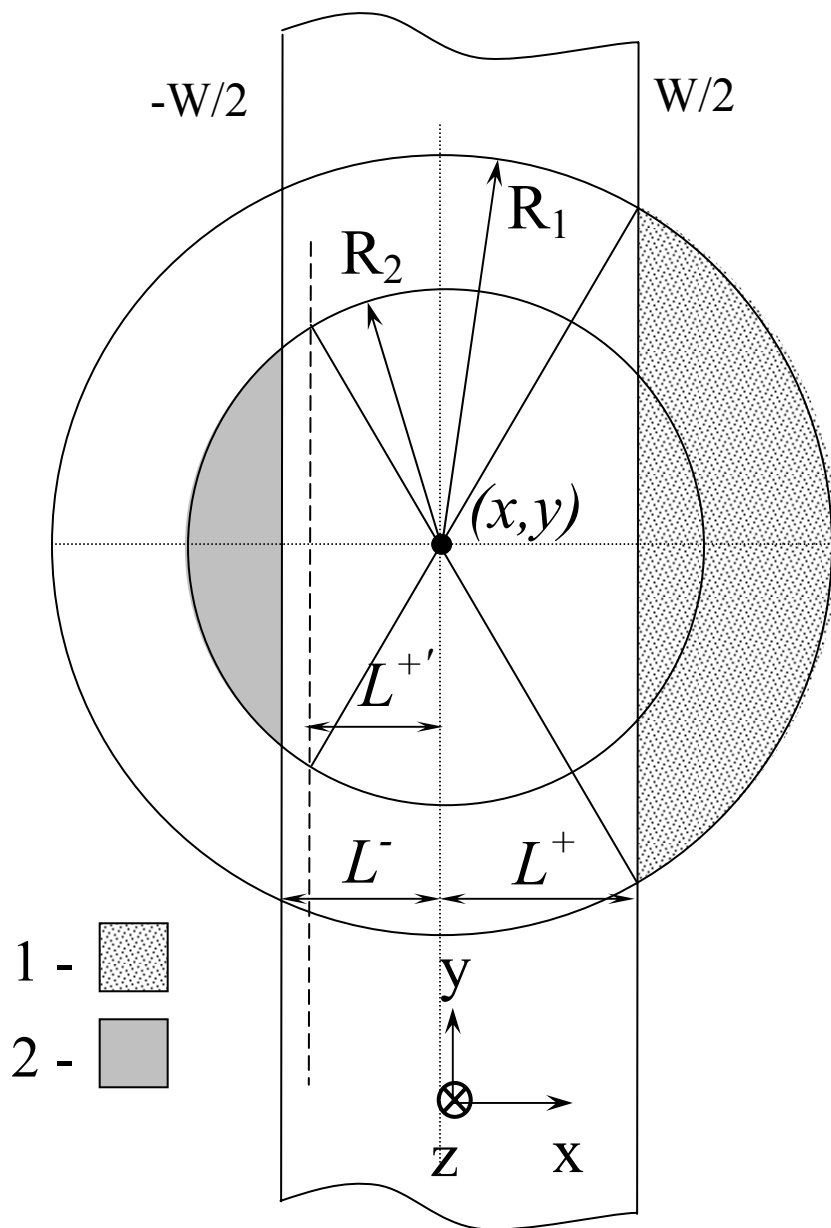


Fig. 22.a

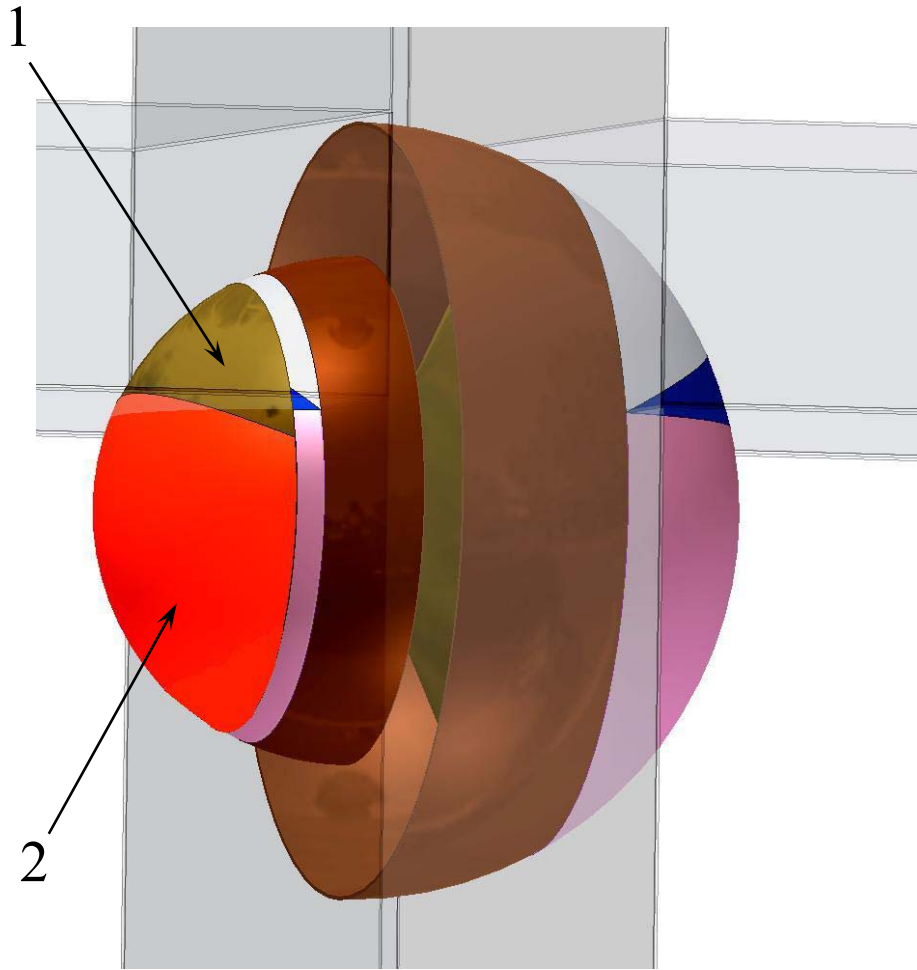


Fig. 22.b

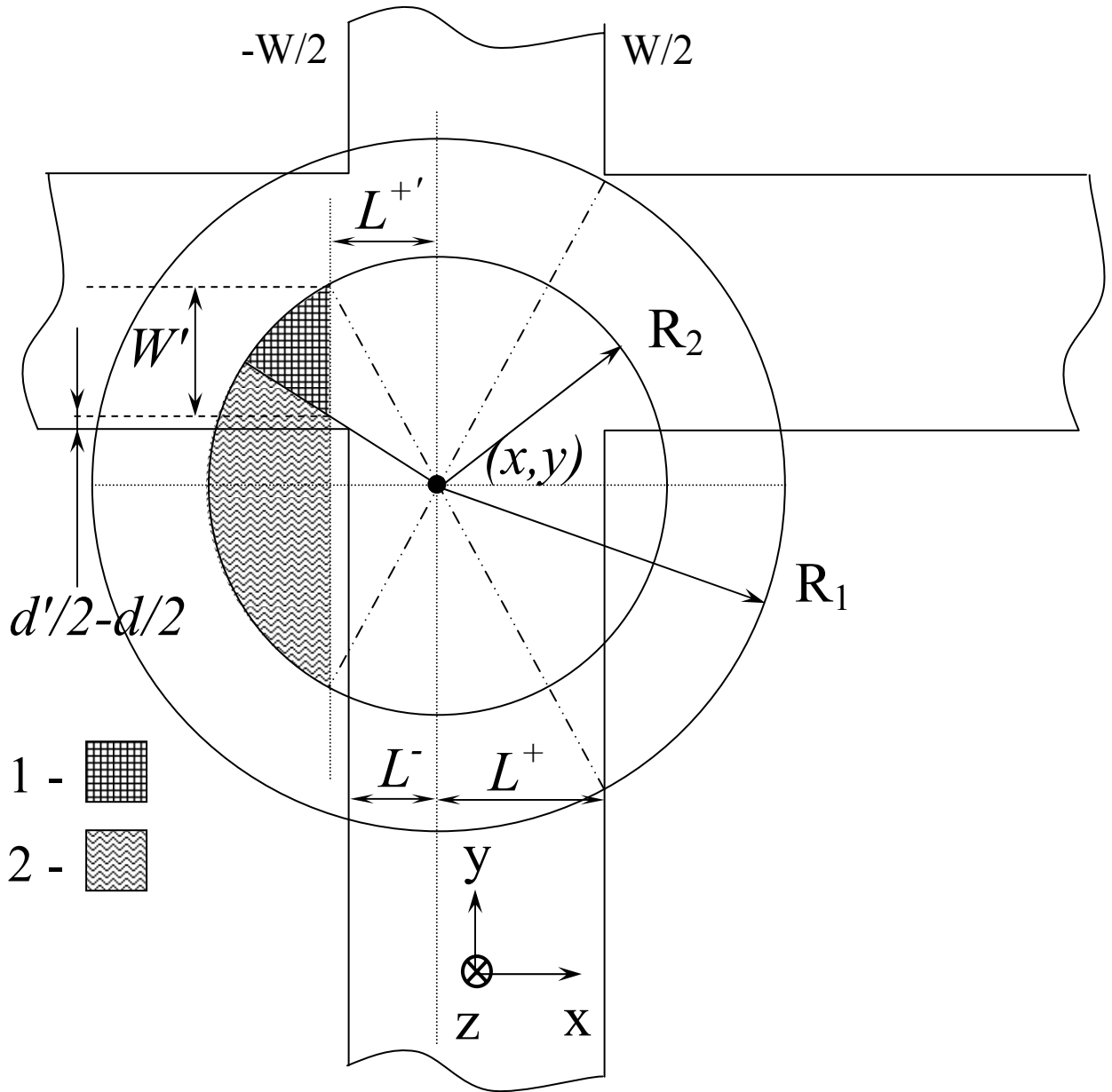


Fig. 22.c

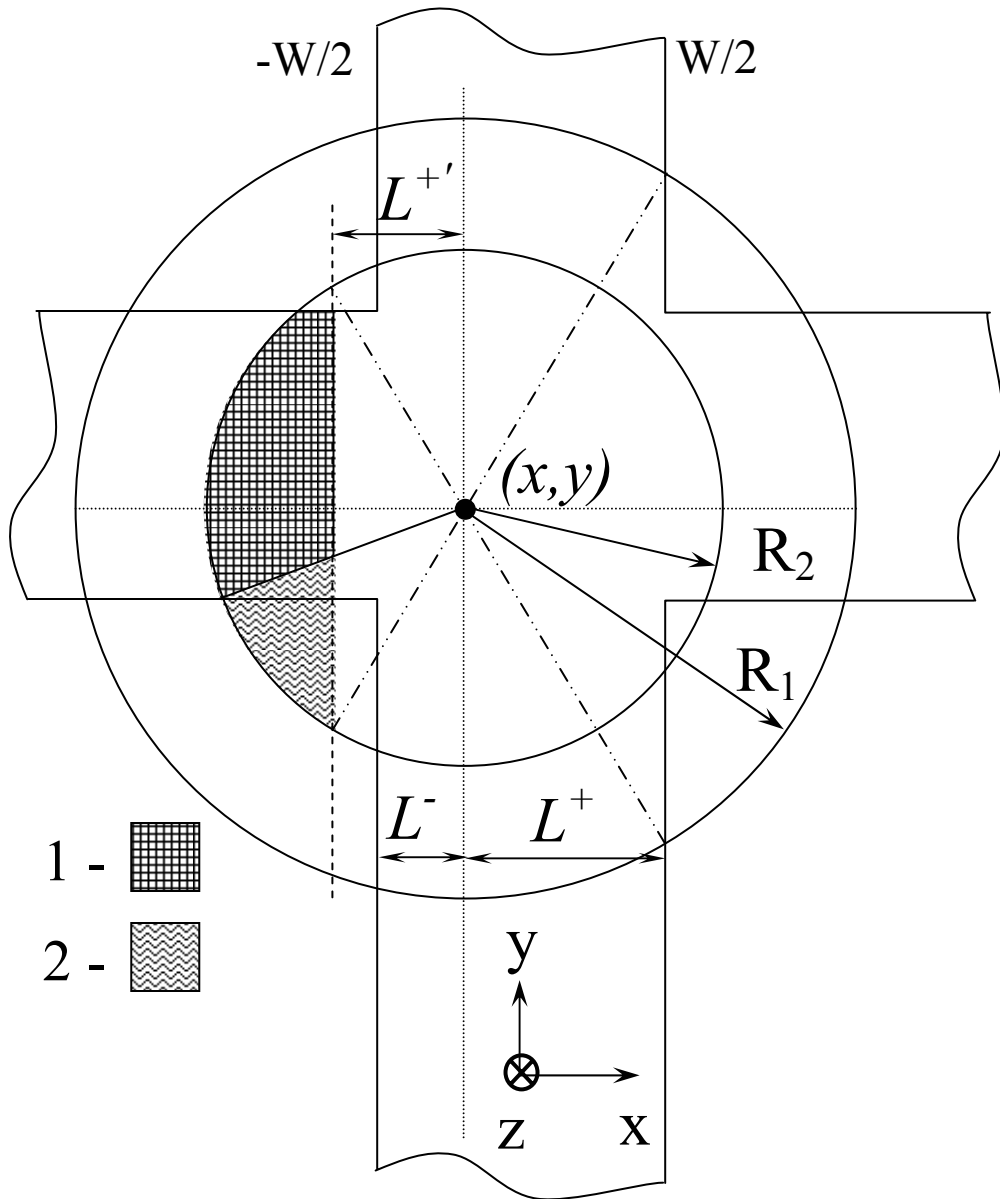


Fig 23.a

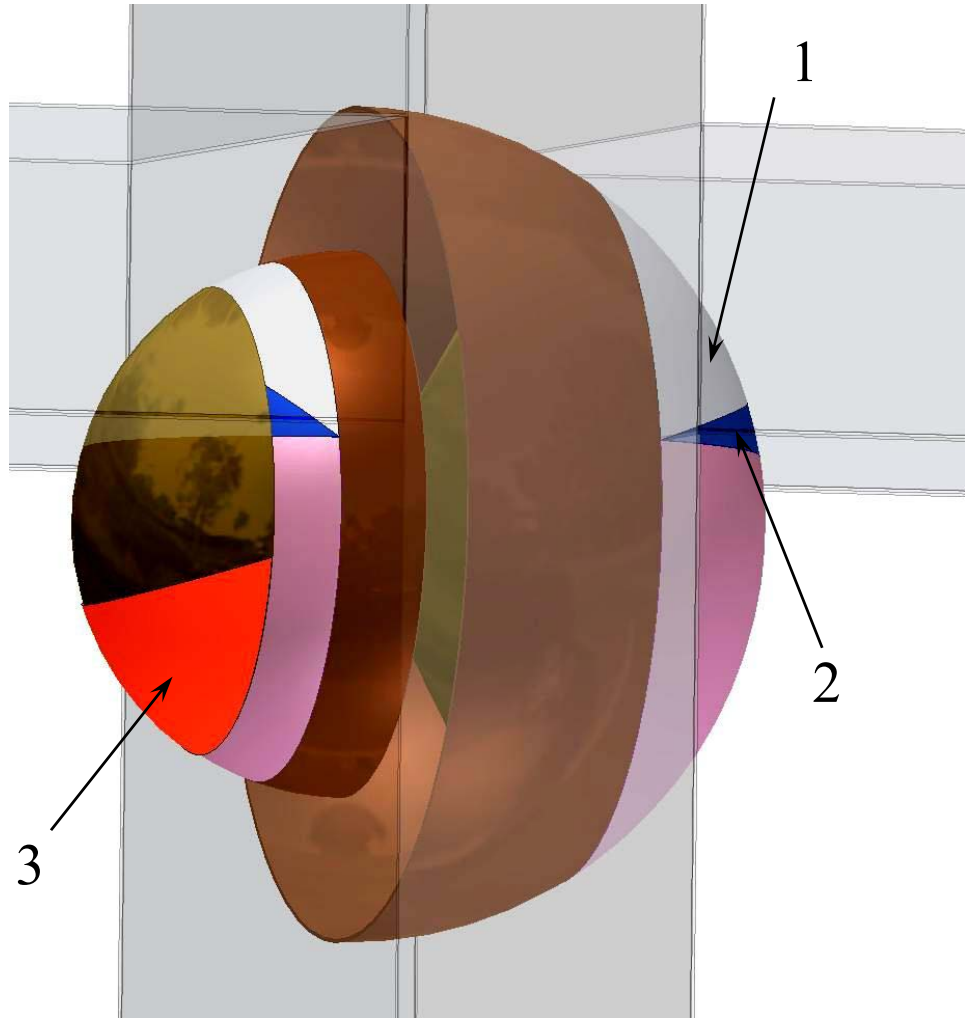


Fig. 23.b

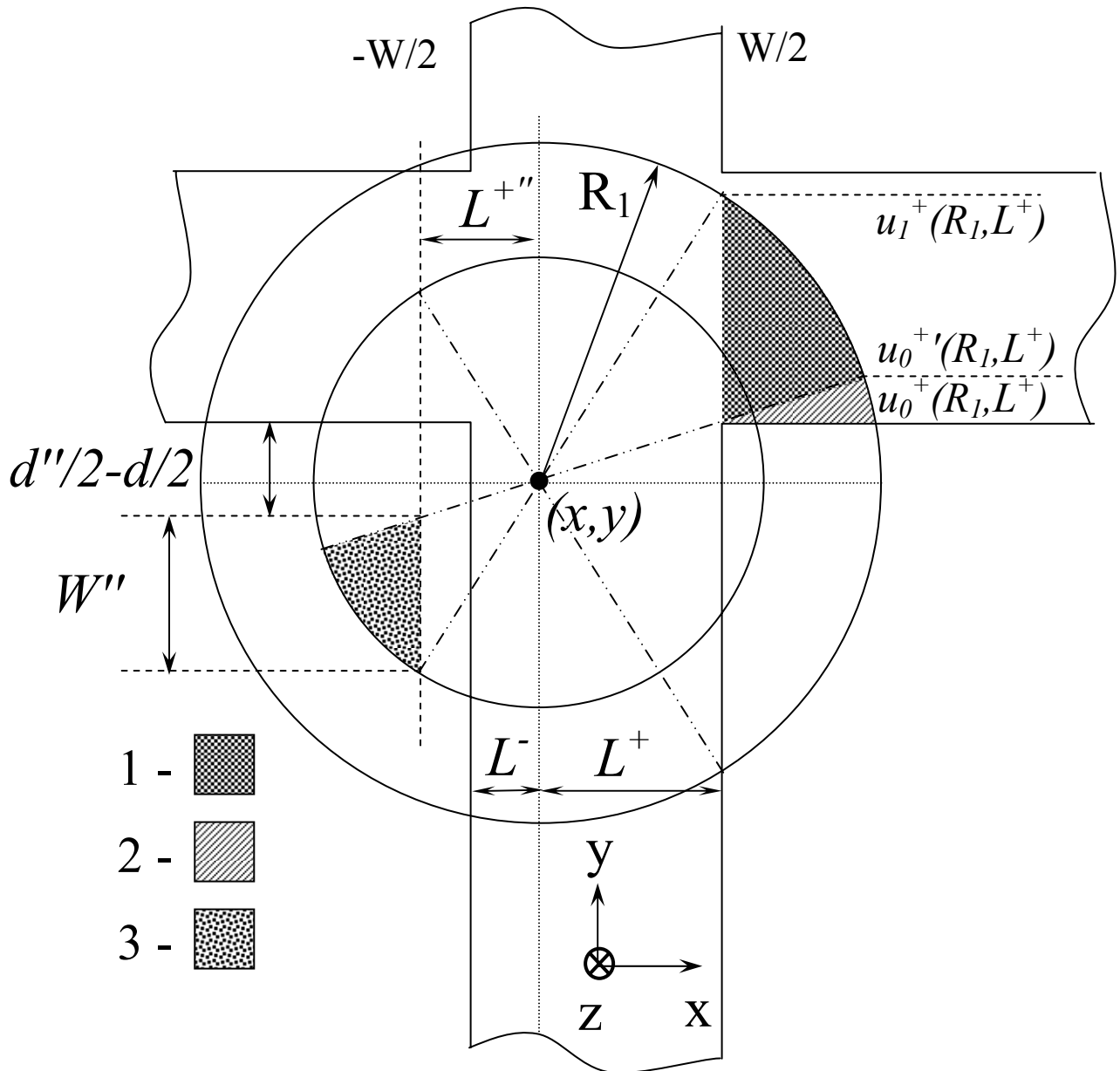


Fig. 23.c

